ARTICLES
https://doi.org/10.1038/s41563-020-00818-y

nature materials

Local negative permittivity and topological phase transition in polar skyrmions

S. Das[1,2,14] ✉, Z. Hong[3,4,14], V. A. Stoica[3,14], M. A. P. Gonçalves[5,6,7,14], Y. T. Shao[8], E. Parsonnet[2], E. J. Marksz[9], S. Saremi[1], M. R. McCarter[2], A. Reynoso[2], C. J. Long[9], A. M. Hagerstrom[9], D. Meyers[1], V. Ravi[1], B. Prasad[1], H. Zhou[10], Z. Zhang[10], H. Wen[10], F. Gómez-Ortiz[6], P. García-Fernández[6], J. Bokor[11], J. Íñiguez[5,7], J. W. Freeland[10], N. D. Orloff[9], J. Junquera[6], L. Q. Chen[3], S. Salahuddin[11], D. A. Muller[8,12], L. W. Martin[1,13] and R. Ramesh[1,2,13] ✉

Topological solitons such as magnetic skyrmions have drawn attention as stable quasi-particle-like objects. The recent discovery of polar vortices and skyrmions in ferroelectric oxide superlattices has opened up new vistas to explore topology, emergent phenomena and approaches for manipulating such features with electric fields. Using macroscopic dielectric measurements, coupled with direct scanning convergent beam electron diffraction imaging on the atomic scale, theoretical phase-field simulations and second-principles calculations, we demonstrate that polar skyrmions in $(PbTiO_3)_n/(SrTiO_3)_n$ superlattices are distinguished by a sheath of negative permittivity at the periphery of each skyrmion. This enhances the effective dielectric permittivity compared with the individual $SrTiO_3$ and $PbTiO_3$ layers. Moreover, the response of these topologically protected structures to electric field and temperature shows a reversible phase transition from the skyrmion state to a trivial uniform ferroelectric state, accompanied by large tunability of the dielectric permittivity. Pulsed switching measurements show a time-dependent evolution and recovery of the skyrmion state (and macroscopic dielectric response). The interrelationship between topological and dielectric properties presents an opportunity to simultaneously manipulate both by a single, and easily controlled, stimulus, the applied electric field.

Spatially complex, real-space topological configurations and their phase transitions have recently emerged as a fertile playground in condensed matter physics[1–4]. Although the focus has been on spin textures in magnets[4–6], leading to the formation of skyrmions and related topologically protected states, in recent years there has been renewed efforts to discover analogous charge textures in, for example, ferroelectrics[7–10]. With the discovery of such polar textures (for example, vortices and skyrmions), it is of both fundamental and practical interest to understand the microscopic and macroscopic nature of their dielectric response and explore the possibility of a field-driven topological phase transition[1,2].

In parallel, the possibility of capturing 'negative permittivity' states in ferroelectrics, either in the temporal (that is, dynamical) or spatial (that is, in equilibrium) domain, has drawn the attention of scientists and engineers alike[11–19]. The concept of negative capacitance was developed in monodomain ferroelectric capacitors by considering that upon transitioning to a ferroelectric state, a material develops a classic 'double-well potential energy' landscape. The minima of these wells represent the equilibrium state of the material and the curvature of the energy landscape dictates that small electric field perturbations should give rise to a classical positive capacitive response (that is, positive permittivity). It was proposed, however, that if one could place the material in the region between these two states (that is, in a region of negative curvature of the energy landscape), it could give rise to a negative capacitive response (that is, negative permittivity) under electric field excitation[2,20]. In a capacitor heterostructure comprising an ideal ferroelectric capacitor (capacitance C_F) in series with a regular dielectric capacitor (capacitance C_D), the overall capacitance $C=(C_F^{-1}+C_D^{-1})^{-1}$ has to be positive for thermodynamic stability. But if $C_F<0$, the total C will be larger than either of the two constituent capacitors taken independently. Accessing this regime, however, remains a challenge in the static sense[14,16,18]: if the capacitor is driven by a voltage, the region of negative curvature is unstable. Researchers have explored approaches wherein the capacitor is driven by a charge that can be simply controlled in an electrostatically coupled ferroelectric/dielectric series capacitor[13]. If it is a dielectrically stiff material, it will effectively suppress the spontaneous polarization of the ferroelectric and thus stabilize the paraelectric state even if the ferroelectric is below its nominal transition temperature[18]. The negative capacitance effect was first proposed in ferroelectric bilayers[11] as well as in several ferroelectrics as transient states[21,22]. Recent work has further demonstrated that

[1]Department of Materials Science and Engineering, University of California, Berkeley, CA, USA. [2]Department of Physics, University of California, Berkeley, CA, USA. [3]Department of Materials Science and Engineering, The Pennsylvania State University, University Park, PA, USA. [4]Department of Mechanical Engineering, Carnegie Mellon University, Pittsburgh, PA, USA. [5]Materials Research and Technology Department, Luxembourg Institute of Science and Technology (LIST), Esch/Alzette, Luxemburg. [6]Departamento de Ciencias de la Tierra y Física de la Materia Condensada, Universidad de Cantabria, Cantabria Campus Internacional, Santander, Spain. [7]Physics and Materials Science Research Unit, University of Luxembourg, Belvaux, Luxembourg. [8]School of Applied and Engineering Physics, Cornell University, Ithaca, NY, USA. [9]National Institute of Standards and Technology, Boulder, CO, USA. [10]Advanced Photon Source, Argonne National Laboratory, Argonne, IL, USA. [11]Department of Electrical Engineering and Computer Sciences, University of California, Berkeley, CA, USA. [12]Kavli Institute at Cornell for Nanoscale Science, Ithaca, NY, USA. [13]Materials Sciences Division, Lawrence Berkeley National Laboratory, Berkeley, CA, USA. [14]These authors contributed equally: S. Das, Z. Hong, V. A. Stoica, M. A. P. Gonçalves. ✉e-mail: sujitdas@berkeley.edu; rramesh@berkeley.edu

in multidomain ferroelectric polar structures, such as the vortices found in $(PbTiO_3)_n/(SrTiO_3)_n$ superlattices, the complex polar order, while producing an overall positive dielectric permittivity, exhibits regions of varying dielectric susceptibility, including areas of local negative capacitive response in the $PbTiO_3$ layers[2].

The recent discovery of chiral polar skyrmions in $(PbTiO_3)_n/(SrTiO_3)_n$ superlattices by the interplay of elastic, electrostatic and gradient energies with a topological number of +1 raises a fundamentally important question: do such skyrmions also exhibit a spatial distribution of varying dielectric susceptibility?[1] Here, we demonstrate a strong enhancement of the out-of-plane dielectric permittivity and that this is a direct consequence of a negative permittivity region that forms at the periphery of each skyrmion. In this region, the polarization is more susceptible to external stimuli than the inner core or the outer regions of the skyrmions. This is further confirmed by second-principles calculations, phase-field modelling and direct microscopic measurements of the local potential energy by scanning convergent beam electron diffraction (SCBED) experiments using an electron microscopy pixel array detector (EMPAD). The macroscopic permittivity also exhibits a large electric field tunable response, which arises from the conversion of the skyrmions into a uniformly polarized state (topological phase transition), as evidenced by both electric field- and temperature-dependent dielectric measurements and synchrotron-based diffraction studies, which are supported by second-principles calculations and phase-field simulations.

Macroscopic details of negative capacitance in polar skyrmions

A series of $[(PbTiO_3)_{16}/(SrTiO_3)_{16}]_m$ superlattices ($m = 3$, 5, 8) and $(SrTiO_3)_{16}/(PbTiO_3)_{16}/(SrTiO_3)_{16}$ trilayers (where the subscript numbers refer to the number of unit cells) as well as 50-nm-thick $SrTiO_3$ and 50-nm-thick $PbTiO_3$ single-layer thin films all grown on TiO_2-terminated single crystalline $SrTiO_3$ (001) substrates, with epitaxial $SrRuO_3$ top and bottom electrodes (all the films were produced by reflection high-energy electron diffraction (RHEED)-assisted pulsed laser deposition; Methods) were synthesized for this study[1]. Plan-view scanning transmission electron microscopy (STEM) images of the superlattices revealed an array of skyrmion bubbles (8–9 nm in diameter; Extended Data Fig. 1a), the formation of which was confirmed by second-principles calculations (Extended Data Fig. 1b)[1], which revealed that they are indeed electric analogues of magnetic skyrmions and have a mathematically definable and characteristic skyrmion number of +1 (Supplementary Table 1). Three-dimensional reciprocal space mapping (RSM) studies of the superlattices about the (002) diffraction condition showed satellite peaks around the film peak along the in-plane directions (side lobes), corresponding to an ordered phase (that is, the skyrmion phase) with a periodicity of 8–9 nm (Extended Data Fig. 2)[1]. In all the heterostructures studied, that is, the superlattices, trilayers and single-layer films, all the layers were found to be coherently strained to the underlying $SrTiO_3$ substrate, confirming that the strain state in all cases is the same. Macroscopic measurements of the dielectric permittivity (extracted from the experimentally measured capacitance, Fig. 1a) and dielectric loss (Extended Data Fig. 3) as a function of electric field (applied normal to the surface) for the $[(PbTiO_3)_{16}/(SrTiO_3)_{16}]_m$ superlattices ($m = 3$, 5, 8) and $(SrTiO_3)_{16}/(PbTiO_3)_{16}/(SrTiO_3)_{16}$ trilayers were completed. The superlattices and trilayer exhibited a strong enhancement of zero-field dielectric permittivity compared with the single-layer $SrTiO_3$ and $PbTiO_3$ heterostructures (Fig. 1a), contrary to what was expected to be a decrease in the overall permittivity as calculated using a conventional 'dielectrics in series' scenario ('series permittivity' is represented by the dotted line in Fig. 1a and Extended Data Fig. 4). These structures also show large electric field tunability (~70–80% for the various superlattices and trilayers in a field of 1,500 kV cm^{-1}), which is notably different from that of single-layer $SrTiO_3$ (~7% under 700 kV cm^{-1}) and $PbTiO_3$ (~2% under 700 kV cm^{-1}; Fig. 1a), as well as polar vortices (which form when the superlattice is synthesized on $DyScO_3$ (110)), which show electric field tunability of almost 45% (Extended Data Fig. 4 and Supplementary Table 2)[2].

Phase-field and second-principles calculations and theoretical rationalization

To understand the microscopic origins of the dielectric observations, we carried out detailed phase-field simulations and second-principles calculations on $[(PbTiO_3)_{16}/(SrTiO_3)_{16}]_8$ superlattices to extract measures of the dielectric permittivity (Methods and Supplementary Fig. 1). The normalized electric field-dependent permittivities derived from both these theoretical approaches (red and green dashed lines, respectively, Fig. 1b) closely resemble the experimental data. The origin of such an enhancement in the dielectric permittivity can be unravelled from the theoretical simulations, which provide spatially resolved maps of the local permittivity (Fig. 2). Taking a real-space representation of the skyrmions (Fig. 2a, left), we can extract the corresponding spatial distribution of the dielectric permittivity within the $PbTiO_3$ layer from the phase-field simulations (Fig. 2a, right). This indicates an unusual dielectric state within the $PbTiO_3$ layer wherein there are regions of negative permittivity (blue/cyan regions, Fig. 2a and Supplementary Fig. 2) at the wall of the skyrmion. Inside and outside this surface region, the permittivity is positive (yellow regions, Fig. 2a). The inverse of the dielectric permittivity derived from the second-principles calculations for a single skyrmion (Fig. 2b and Supplementary Fig. 3) also reveals the existence of a region of negative permittivity at the periphery of the skyrmions. The corresponding electric susceptibility (Fig. 2c and Supplementary Fig. 3) also reveals that the wall of the skyrmion exhibits the highest electric susceptibility and deforms with an applied electric field to increase/decrease the volume of the core.

Based on these calculations, it is possible to reconstruct the macroscopic dielectric permittivity of the $[(PbTiO_3)_{16}/(SrTiO_3)_{16}]_8$ superlattice (Supplementary Note 1 and schematically illustrated in Fig. 2d). Although the superlattices consist of $SrTiO_3$ and $PbTiO_3$ layers connected in series, the $PbTiO_3$ layers have two regions, one inside/outside the skyrmions with positive permittivity and the other at the wall of the skyrmions with negative permittivity, which are electrically parallel to each other (Fig. 2d). Based on this structure, an 'effective circuit' model for this stack (Fig. 2d, right) enabled us to calculate the net permittivity of the superlattice as a function of the individual dielectric permittivities of $SrTiO_3$ (ε_1), $PbTiO_3$ within/without the skyrmion (ε_2) and $PbTiO_3$ within the skyrmion boundary (ε_3; Fig. 2e,f). There are a few key conclusions that emerge from these calculations: for normal values of the permittivity of $SrTiO_3$ and $PbTiO_3$ (that is, values less than 300), the permittivity of the skyrmion wall (ε_3) is negative (Fig. 2e,f) to obtain an effective dielectric permittivity of the superlattice of around 800, consistent with the results shown in Fig. 1a. Positive values of the skyrmion wall permittivity can be obtained from non-reasonable values of the permittivity of the $SrTiO_3$ and $PbTiO_3$ layers, for example, identified by data points with fictitious permittivities (Fig. 2e). These scenarios seem unlikely because it would mean that simultaneously, both $SrTiO_3$ and the $PbTiO_3$ layer as a whole have a substantially enhanced permittivity compared with that in the bulk (Supplementary Note 1). Based on these calculations and the experimental measurements, we estimate the permittivity of the skyrmion wall to be around −900, which is qualitatively consistent with phase-field simulations and second-principles calculations (Fig. 2a–c). Comparisons of the dielectric permittivity of the vortex and the skyrmion (Extended Data Fig. 4) show that they are notably different from each other. We note that although large enhancements in dielectric permittivity have been observed in other systems (for example, relaxor ferroelectrics and functionally graded

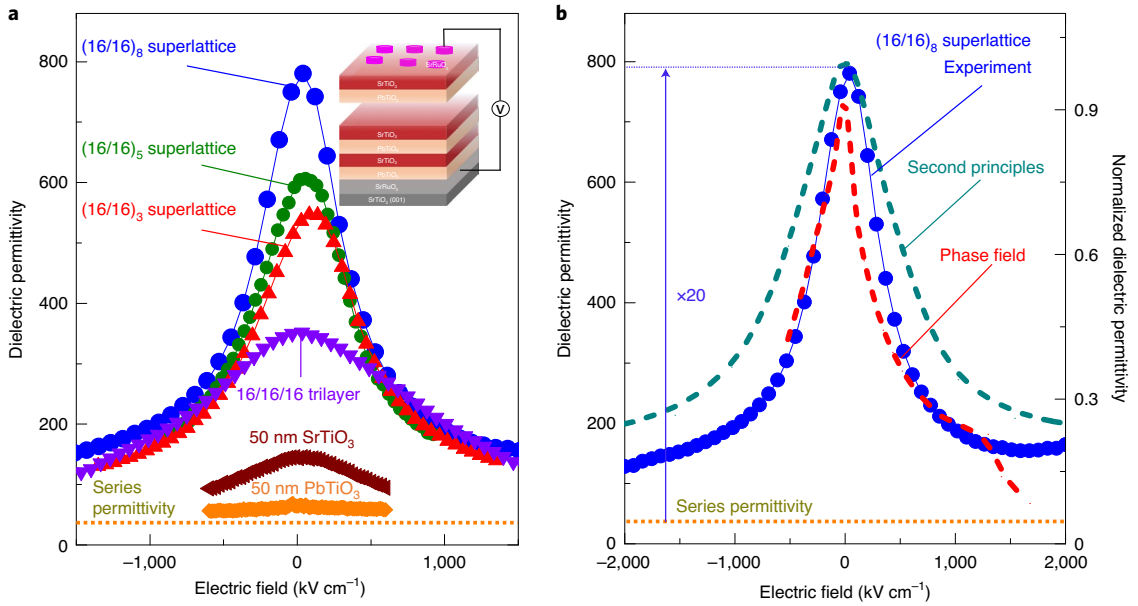

Fig. 1 | Macroscopic demonstration of stabilization of the negative capacitance of polar skyrmions. a, The dielectric permittivity as a function of electric field (applied voltage divided by the thickness of the sample) for $[(SrTiO_3)_{16}/(PbTiO_3)_{16}]_8$, $[(SrTiO_3)_{16}/(PbTiO_3)_{16}]_5$ and $[(SrTiO_3)_{16}/(PbTiO_3)_{16}]_3$ superlattices and $(SrTiO_3)_{16}/(PbTiO_3)_{16}/(SrTiO_3)_{16}$ trilayer, which are in the skyrmion state in contrast to their constituents (50 nm $SrTiO_3$ and 50 nm $PbTiO_3$ single layers). The horizontal yellow dotted line shows the effective permittivity at zero field (~37), derived from the series combination of effective 50 nm $SrTiO_3$ and 50 nm $PbTiO_3$ layers. Inset: schematic of the measured sample geometry. **b**, Left axis: the experimentally measured relative dielectric permittivity of the $[(SrTiO_3)_{16}/(PbTiO_3)_{16}]_8$ superlattice (blue dots) as a function of electric field is enhanced compared with the series permittivity (horizontal yellow dotted line) at zero field (~37). An enhancement in permittivity of almost 20-fold is observed compared with this threshold, caused by a stabilized negative capacitance (permittivity) in the $PbTiO_3$ layer. Right axis: the normalized dielectric permittivities derived from phase-field simulations (red dashed line) and second-principles calculations (green dashed line) closely resemble the experimentally measured normalized electric field-dependent permittivity (blue dots). The results have been rescaled and the normalization carried out with respect to the zero-field value.

ferroelectrics)[23], the fundamental physical origins of the enhancement in the dielectric response in this case is completely different from other possible phenomena (for example, Maxwell–Wagner effects, inductor–capacitor (LC) resonance)[24–26], again suggesting that it is intimately associated with the skyrmion state. The measured out-of-plane capacitance (permittivity; Extended Data Fig. 5) shows a linear-logarithmic frequency dependence, decreasing by approximately 4% per decade across the measured range from 10^2 to 10^6 Hz. Theoretical models of the electrodynamics of ferroelectric thin films with negative capacitance suggest that the strongest variations with respect to the static limit should appear in the resonance THz regime, orders of magnitude larger than the ones explored in the present work[27]. This behaviour is not present in the measured capacitance and permittivity of the single-composition $PbTiO_3$ and $SrTiO_3$ films, and therefore likely indicates dynamic effects of the skyrmions at these frequencies (details of the frequency dependence of in-plane capacitance and permittivity are presented in Extended Data Fig. 6 and Supplementary Note 2)[28,29].

Microscopic observation of negative capacitance at skyrmion walls

The possibility of the existence of such a region of negative permittivity at the skyrmion wall and the potential energy landscape across the skyrmion can be directly probed by SCBED experiments. These imaging experiments were carried out in cross-section samples so that we could image both the Neél and Bloch components edge-on (Fig. 3a)[1]. The SCBED experiments were performed using an EMPAD (Supplementary Fig. 4 and Methods), which records the full momentum distribution (that is, the electron diffraction pattern) at every scan position, providing information to measure both the ferroelectric polarization and electric field simultaneously and independently (Fig. 3b–d). For this study, we focused on the deflection of the (000) beam because there are fewer polarity effects. The polarization direction is quantitatively determined from the diffraction intensity differences of Friedel pairs, such as (100)/($\bar{1}$00) and (001)/(00$\bar{1}$) for the x and z components of polarity, respectively (Fig. 3b, Supplementary Fig. 4 and Methods)[2]. Long-range electric fields can be reconstructed from the deflection of the entire convergent beam electron diffraction (CBED) pattern by the Lorentz force (Fig. 3c, Supplementary Fig. 4 and Methods)[2,30]. Focusing along the dashed horizontal line profile (Fig. 3b,c) that passes through the centre of a skyrmion, we can extract information about the walls of the skyrmion (Fig. 3a)[1] by measuring the polarization (P_z) and electric field (E_z) along this line (Fig. 3d). The magnitude of the measured polarization was calibrated using the polarization of $PbTiO_3$ as reference[31]. With both the measured electric field and polarization, we can estimate the local potential energy of the system following the approach given in ref. [2]. The estimated potential energy (G) as a function of P_z across the skyrmion (Fig. 3e; for details, see Methods) reveals the existence of local potential energy maxima ($\partial^2 G/\partial P^2 < 0$) at the skyrmion wall, where P_z is small (Fig. 3e). This supports the existence of regions having negative curvature of free energy (that is, negative permittivity) at the skyrmion walls.

Field- and temperature-driven permittivity and topological phase transition

Having identified a possible source of the enhancement of overall permittivity associated with the negative permittivity at the skyrmion wall, we now discuss the changes in the dielectric response and the topological structure induced by an electric field (Fig. 4). Both phase-field simulations and second-principles calculations revealed that when an electric field is applied along the out-of-plane

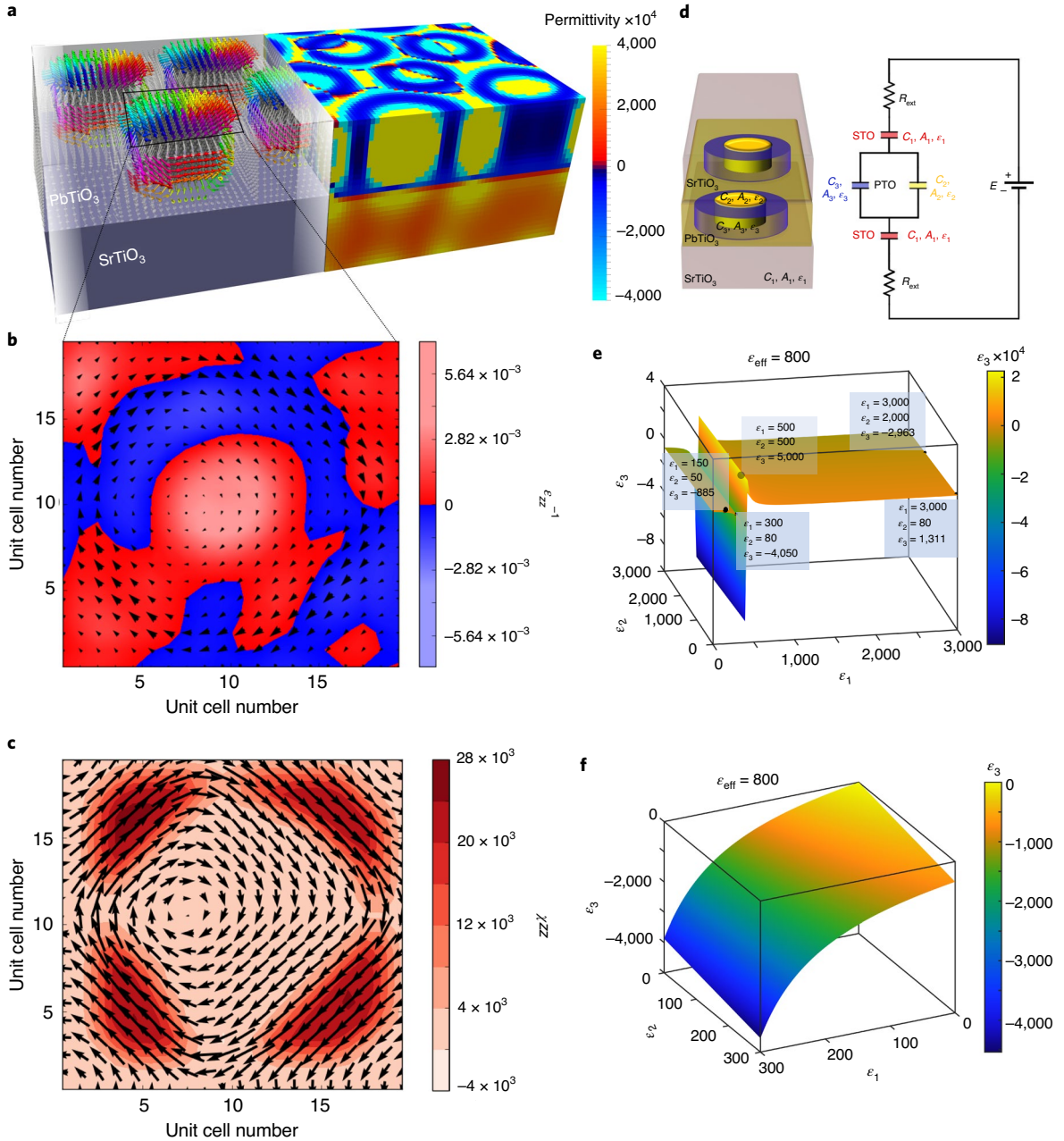

Fig. 2 | Phase-field, second-principles and macroscopic calculations of the negative permittivity of the skyrmion structure at 300 K in a $[(SrTiO_3)_{16}/(PbTiO_3)_{16}]_8$ superlattice. a, Second-principles calculations of the skyrmion structure (left) and phase-field simulated spatial map of the permittivity of the central $PbTiO_3$ layer of the skyrmion (right), presenting evidence of local negative permittivity regions (blue contrast). **b**,**c**, Second-principles calculations of the two-dimensional distribution of the inverse of the dielectric permittivity (**b**) and the susceptibility at the central plane of $PbTiO_3$ (**c**) showing the Bloch-like skyrmion texture. Both were computed according to ref. [2], and the colour codes with key are presented on the right. Both **b** and **c** are overlaid by polarization vectors. The arrows represent the components of the polarization in the *x*–*y* plane of the skyrmion. **d**, Macroscopic illustration of our $PbTiO_3$/$SrTiO_3$ system (left, details in Methods) and the corresponding circuit diagram (right). R_{ext} describes some external resistance of the circuit leading up to the thin-film capacitor, for example, from the electrodes. STO, $SrTiO_3$; PTO, $PbTiO_3$. **e**, Calculations of the permittivity of the skyrmion wall (ε_3) as a function of ε_1 and ε_2 based on the model described in **d**. A three-dimensional (3D) plot of the interdependence between ε_1, ε_2 and ε_3, constrained by an effective dielectric permittivity (ε_{eff}) of 800 (to match the experimental results in Fig. 1a and Supplementary Note 1). The permittivity of the skyrmion wall is always negative except for non-reasonable values of the permittivity of the $SrTiO_3$ and $PbTiO_3$ layers, for example, identified by data points with fictitious permittivities. These fictitious scenarios are unlikely because it would mean that both $SrTiO_3$ and $PbTiO_3$ have a substantially enhanced permittivity compared with that in the bulk. **f**, A section of the phase space in **e**, showing the permittivity of the skyrmion wall (ε_3) as a function of ε_1 and ε_2 specifically for values of $SrTiO_3$ and $PbTiO_3$ layer permittivities in the range 0–300 (which is a reasonable range for thin films), showing that the wall permittivity is negative over the entire range.

direction (parallel/antiparallel to the uniform polarization of the skyrmion cores), the skyrmions progressively expand (shrink) for parallel (antiparallel) fields and ultimately the entire material becomes uniformly poled with increasing electric field (Fig. 4a–c and Extended Data Figs. 7 and 8). To validate these calculations, we performed electric field-dependent X-ray diffraction RSM studies

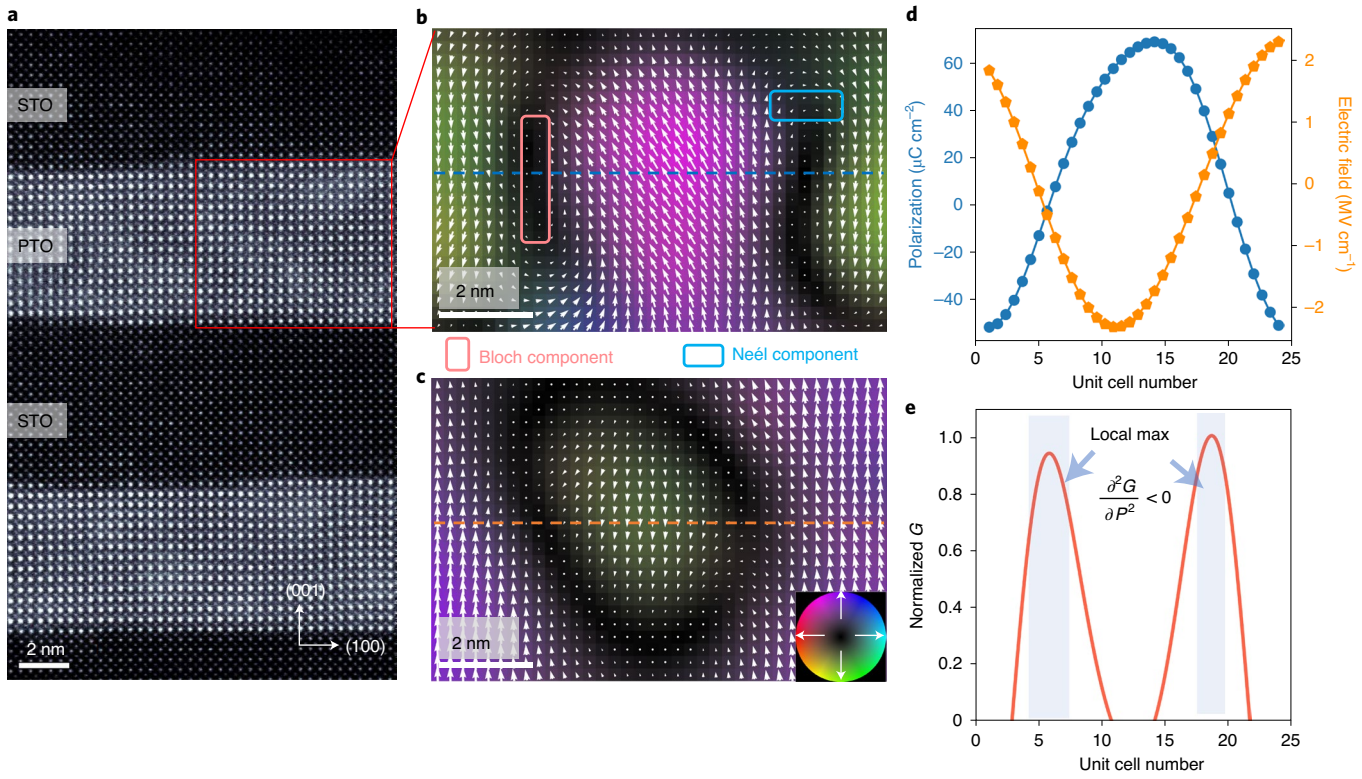

Fig. 3 | Measurement of local polarization, electric field and local potential energy of the polar skyrmion using SCBED. a, A cross-sectional high-angle annular dark-field STEM image of the skyrmions in the $PbTiO_3$ layer. **b**,**c**, Polarization (**b**) and electric field (**c**) vector maps of the cross-section geometry (*x*–*z* plane) of the skyrmion measured using SCBED. We can access the Neél (blue box) and Bloch (red box) components from the skyrmion cross-section. The out-of-plane polarizations are separated by in-plane Bloch chiral domain walls (dark regions). The colour wheel hue (saturation) in **c** corresponds to the direction (magnitude) of the in-plane component of the ferroelectric polarization. **d**, Variation of the *z* components of the local polarization (P_z; blue curve) and electric field (E_z; orange curve) along a horizontal line drawn through the centre of a polar skyrmion, indicated by the dashed lines in **b** and **c**. **e**, Local potential energy estimated from the variation in P_z and E_z along the same line. Regions around the skyrmion walls (indicated by arrows) have a local energy higher than the surroundings with a negative curvature ($\partial^2 G/\partial P^2 < 0$), indicating local negative permittivity.

(Methods) to observe the skyrmion evolution[1] as a function of the applied electric field. These studies (Fig. 4d–f and Supplementary Fig. 5) showed the systematic disappearance of the skyrmion satellite peaks with increasing electric field, indicating field-induced structural changes related to the skyrmions (Fig. 4e–f, Extended Data Fig. 9a–c and Supplementary Figs. 5 and 6). The external electric field in the out-of-plane direction breaks the symmetry and tends to align the dipoles along the direction of the external field to minimize the energy[32,33]. The electric field-driven change in the size of the skyrmion directly impacts the effective dielectric permittivity as well as the negative component of permittivity (Supplementary Note 3, Extended Data Fig. 9d and Supplementary Fig. 7). The calculated and experimentally measured dielectric permittivities are in close quantitative agreement. Also, the normalized intensities of the skyrmion satellite peaks closely resemble the trends in the evolution of the electric field dependence of the permittivity (dark grey; Extended Data Fig. 9e). The same trend is observed in the temperature-dependent change of the effective dielectric permittivity of the superlattice (Extended Data Fig. 10), which closely follows the experimentally measured temperature-dependent permittivity.

Such polar skyrmions are characterized mathematically by the topological charge/number, $N_Q = \frac{1}{4\pi}\int \mathbf{u} \cdot \left(\frac{\partial \mathbf{u}}{\partial x} \times \frac{\partial \mathbf{u}}{\partial y}\right) dxdy$, where $\mathbf{u}$ denotes the normalized local dipole moment, and the surface integral is taken over the corresponding (001) plane. The integrand is the Pontryagin density, and its surface integral is the topological number of the observed skyrmion, which takes an integer value of +1, as confirmed by phase-field simulations and second-principles calculations[1]. Our simulations suggest a topological transition from a skyrmion state to a uniform ferroelectric state at an electric field $\gtrsim$1,500 kV cm^{-1}. Below this threshold, the Pontryagin density is finite (Supplementary Fig. 8) and the topological number remains +1 (Fig. 4g). Above this field, the skyrmion disappears, indicating that the polarization texture is unstable and transforms into a uniform ferroelectric state with a trivial $N_Q = 0$ (Fig. 4g, Extended Data Figs. 7 and 8 and Supplementary Figs. 5 and 6). Thermal excitations induce a similar topological phase transition from the skyrmion state to a uniform ferroelectric state, with a phase field-estimated critical temperature of ~700 K. Experimentally, such phase transitions can be inferred from the presence (skyrmion phase, $N_Q = 1$) or absence (trivial topological phase, $N_Q = 0$) of intensity in the side-lobe satellites in the electric field- (Fig. 4d–g) or temperature-dependent (Fig. 4h and Extended Data Fig. 10) RSMs. The satellite peaks arising from the skyrmions disappear, respectively, at 1,500 kV cm^{-1} and ~600 K, indicating that the topological number has switched from +1 to 0 (Fig. 4 and Extended Data Fig. 10), which, again, agrees qualitatively with the theoretical expectations. The field-driven change to the skyrmion is due to the shrinkage of the volume of the domain with a polarization opposite to the external electric field. For a critical field, the domain will collapse and the transition to a monodomain state is completed. Right before the transition, a singularity appears: the stereographic projection of the dipole pattern does not completely wrap the unit sphere. That is exactly the point at which the skyrmion number changes from +1 (non-trivial

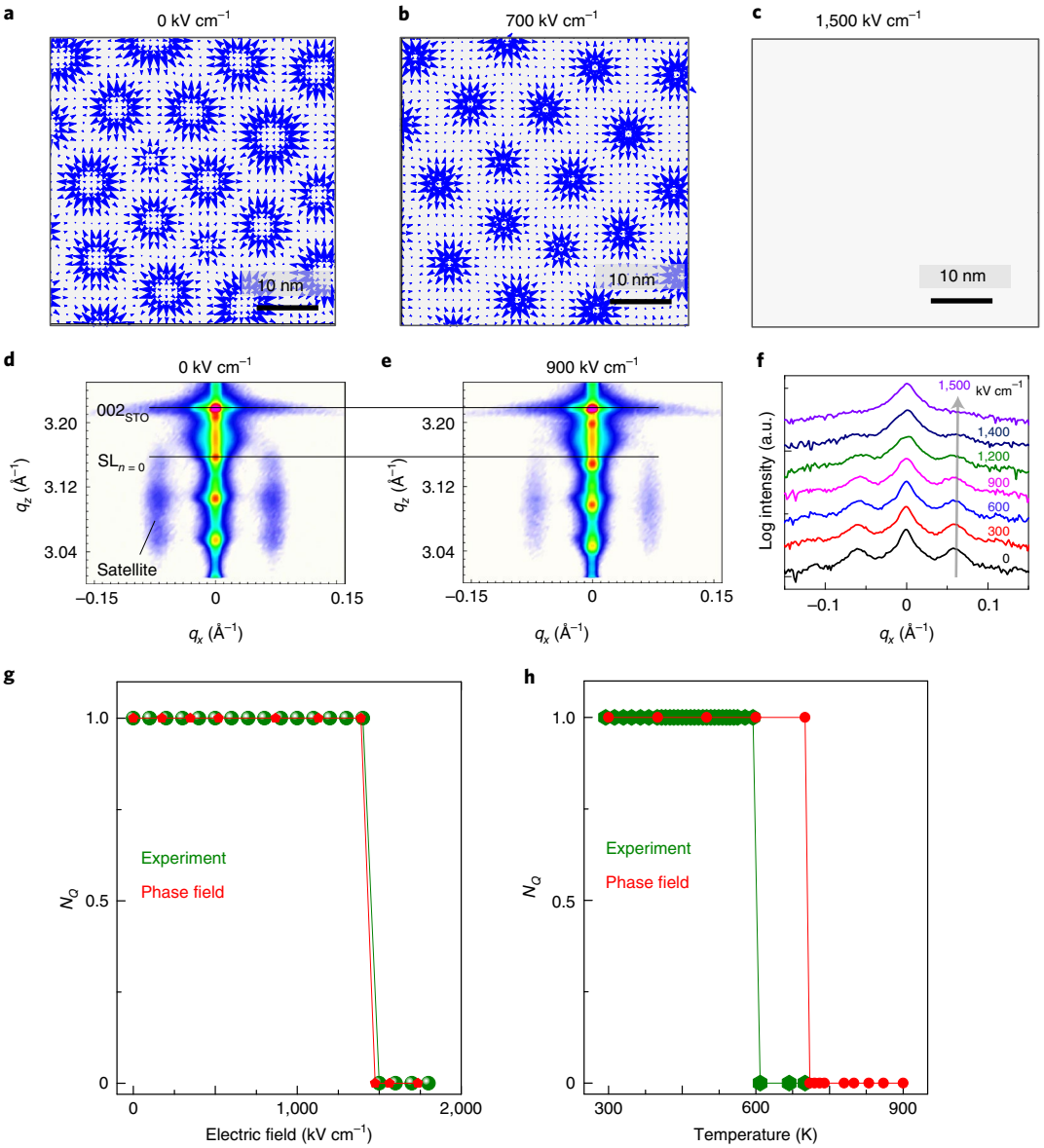

Fig. 4 | Electric field control of the topological phase transition of the polar skyrmion of the $[(SrTiO_3)_{16}/(PbTiO_3)_{16}]_8$ superlattice. a–c, Phase-field simulations show the shrinkage of the diameters of the skyrmions when an electric field is applied, from zero field (**a**) to 700 kV cm^{-1} (**b**), and ultimately the entire sample becomes uniformly ferroelectric at ~1,500 kV cm^{-1} (**c**). **d**,**e**, Electric field-dependent reciprocal space maps show the systematic disappearance of the satellite peaks (side lobes, which correspond to the skyrmions) upon increasing the electric field from zero (**d**) to 700 kV cm^{-1} (**e**); SL indicates the superlattice peak. **f**, The intensity profiles along the reciprocal lattice vector q_x at various electric fields show the disappearance of the skyrmion peaks at ~1,500 kV cm^{-1}. **g**, Dependence of the topological number (N_Q) on electric field. At around +1,500 kV cm^{-1}, the topological number flips from +1 to zero, indicating the topological skyrmion phase transition to the trivial single domain state. The topological numbers from a phase-field simulation (red symbols and line) of the same $(SrTiO_3)_{16}/(PbTiO_3)_{16}$ superlattice closely match the experimental observations (green symbols and line). **h**, Dependence of N_Q on temperature. At ~600 K, the topological number flips from +1 to zero, indicating the topological skyrmion phase transition to the ferroelectric monodomain state (green symbols and line). This observation is slightly different from the phase-field simulation due to strain relaxation (red symbols and line).

topological structure) to 0 (trivial state with a monodomain configuration). Finally, such a field/temperature-driven topological phase transition bears resemblance to that in other magnetic topological structures[4,34–37].

Probing skyrmion dynamics with time-dependent capacitance

To further understand the reversible evolution of these structures under applied electric fields, the temporal evolution of the skyrmion ground state can be probed by perturbing it with electric field pulses that drive the system to a uniform polar state, and then measuring the time-dependent evolution back to the skyrmion state (Fig. 5, Supplementary Figs. 9 and 10, and Methods). Here, we performed two sets of measurements. The first focused on applying strong, unipolar pulses (U_1 and U_2) with varying lengths of delay time (t_d) between the pulses. We measured the current that flows in the capacitor during the application of U_1 (that is, I_1), then allowed possible relaxation to occur during t_d and finally measured the current that flows during the application of U_2 (that is, I_2). Taking the difference $I_1 - I_2$ for various t_d provides a time-dependent measure

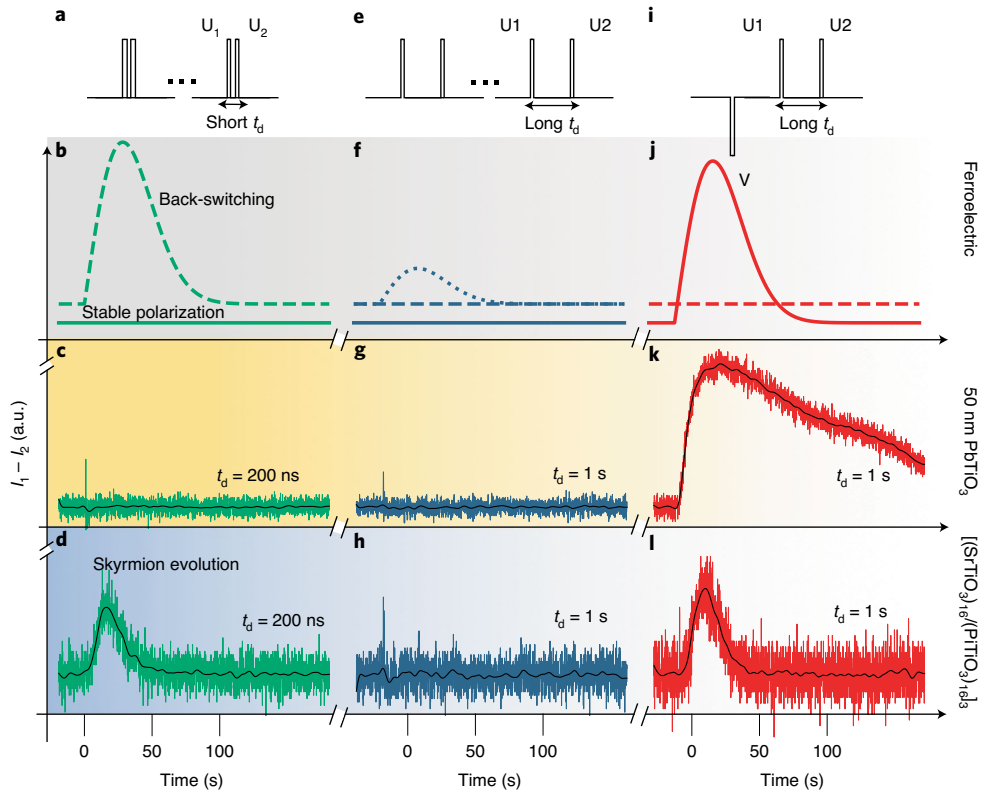

Fig. 5 | Generation of a transient state with time-dependent capacitance under out-of-plane measurement of the skyrmion. a, Schematic of two unipolar pulses (U_1 and U_2) applied to a sample with a short delay time (t_d) between pulses. Application of unipolar pulse U_1 poles the sample to the uniform polarization state. Zero field was applied for time t_d, during which the system relaxes. We monitored the difference in current response to U_1 and U_2 ($I_1 - I_2$) to reveal a transient state after initial poling. **b**, Expected difference in the current response ($I_1 - I_2$) for a ferroelectric with (dashed green line) and without (solid green line) back-switching. **c**, $I_1 - I_2$ for the parent ferroelectric (50 nm $PbTiO_3$ layer), indicating stable polarization. **d**, $I_1 - I_2$ for the superlattice shows a notable peak, suggesting the occurrence of a relaxation process. **e**, To probe the relaxation timescale, we performed the same experiment with a long time delay. **f**, Expected behaviour for a classical ferroelectric with complete back-switching (dashed line), partial back-switching (dotted line) and stable ferroelectric polarization (solid line). **g**, As expected, the parent 50 nm $PbTiO_3$ layer shows a flat line for $I_1 - I_2$, that is, stability. **h**, Notably, the superlattice also shows a flat line for $I_1 - I_2$, indicating that relaxation is complete on this timescale ($t_d = 1$ s shown). **i**, Finally, we performed an experiment in which we also included a preset pulse-down pulse (V) and monitored $I_1 - I_2$ for long t_d. **j**, The ferroelectric back switching is represented by the dashed line and the expected behaviour from a ferroelectric, a switchable, stable polarization (solid line). **k**, The parent 50 nm $PbTiO_3$ layer shows a strong signal coming from the switchable remnant polarization. **l**, The difference in the current response ($I_1 - I_2$) for the skyrmion sample, which importantly shows a distinguishable signal. This, in conjunction with the data in **d** and **h**, indicates that the origin of the relaxation seen in the skyrmion sample is not derived from back-switching of the small remnant polarization, but rather a new mechanism originating in the polar skyrmion structure.

of the amount of relaxation after the poling process. For short delay times ($t_d \lesssim 10\,\mu$s, Fig. 5a and Supplementary Note 4), for the parent 50-nm-thick $PbTiO_3$ film (here, with $t_d = 200$ ns, Fig. 5b,c), a flat, zero response corresponding to stable, poled ferroelectric behaviour was observed. On the other hand, similar experiments on the superlattices with skyrmions (here, with $t_d = 200$ ns, Fig. 5d) revealed a transient peak, suggesting that there is a relaxation process different from that observed in a classical ferroelectric based on the same material (data for other short t_d values are also provided in Supplementary Fig. 10).

To further understand the relaxation processes and, in particular, reveal the timescales over which these processes persist, we carried out similar experiments with progressively longer t_d. Upon transitioning to long delay times ($10\,\mu s \lesssim t_d \lesssim 1$ s, Fig. 5e and Supplementary Note 4), for the parent 50-nm-thick $PbTiO_3$ film (here, with $t_d = 1$ s, Fig. 5f,g), a flat, zero response corresponding to stable, poled ferroelectric behaviour was once again observed. Likewise, similar experiments for the superlattices exhibiting skyrmion structures revealed a flat, zero response, suggesting the relaxation process has been completed within 1 s (here, with $t_d = 1$ s, Fig. 5h and Supplementary Fig. 10).

Thus far, the observations suggest that (not surprisingly) the single-layer parent ferroelectric film remains stable in whatever state it is electrically poled into, whereas the superlattices exhibiting skyrmion structures exhibit relaxation processes. This could correspond to classical back-switching (that is, the applied bias pushes the skyrmion into a uniform polar state, which then relaxes back to a classical up-and-down-poled domain structure) or indicate an exotic relaxation back towards the skyrmion structure. To distinguish between these two cases, we performed a second set of experiments in which we applied a preset pulse V opposite to U_1 and U_2 with a long t_d (Fig. 5i and Supplementary Note 4). When this experiment was performed on the parent 50-nm-thick $PbTiO_3$ film (here, with $t_d = 1$ s, Fig. 5j,k), a non-zero response, corresponding to what is expected for stable, poled ferroelectric behaviour, was observed. This contrasts with the long delay time study without the preset pulse, which showed no peak (Fig. 5g). On the other hand, similar experiments on the superlattices exhibiting skyrmions (here, with $t_d = 1$ s, Fig. 5l) revealed a small transient peak, suggesting that the small remnant polarization of the superlattice can be switched (Supplementary Fig. 9). From other experiments (Fig. 5d,g), it appears that these superlattices relax or back-switch

within ~1 s; however, if this was true, we should have seen no peak in this preset pulse experiment (Fig. 5l). Thus, this is indicative of a totally different relaxation process, that is, it cannot be explained simply by the classical back-switching of a ferroelectric, but instead suggests there is an exotic, time-dependent evolution of the emergent polarization state that we can unravel and then re-establish reversibly.

Our work has demonstrated a direct relationship between the macroscopically measured dielectric permittivity and the microscopically imaged potential energy landscape. Application of an electric field drives the skyrmions into a uniform polar state in a reversible way with an accompanying large tunability of the permittivity as well as a corresponding topological phase transition, which is analogous to what has been observed in the case of magnetic skyrmions and their magnetic field-driven evolution into a uniform magnetic state[38]. The microscopic nature of this reversible recovery of the skyrmion state should be a matter of great interest for future studies[38]. Future electric field-dependent dielectric spectroscopy measurements extending into the infrared frequency regime (IR), combined with new theory, may help connect the frequency dispersion of the dielectric permittivity with the microscopic detail of the skyrmion ensemble. The production of such a steady-state negative capacitance and large field-tunable response has promise for high-frequency electronic applications.

Online content

Any methods, additional references, Nature Research reporting summaries, source data, extended data, supplementary information, acknowledgements, peer review information; details of author contributions and competing interests; and statements of data and code availability are available at https://doi.org/10.1038/s41563-020-00818-y.

Received: 14 September 2019; Accepted: 1 September 2020;
Published online: 12 October 2020

References

1. Das, S. et al. Observation of room temperature polar skyrmions. *Nature* **568**, 368–372 (2019).
2. Yadav, A. K. et al. Spatially resolved steady state negative capacitance. *Nature* **565**, 468–471 (2019).
3. Kosterlitz, J. M. & Thouless, D. J. Ordering, metastability and phase transitions in two-dimensional systems. *J. Phys. C* **6**, 1181–1203 (1973).
4. Nagaosa, N. & Tokura, Y. Topological properties and dynamics of magnetic skyrmions. *Nat. Nanotechnol.* **8**, 899–911 (2013).
5. Rößler, U. K., Bogdanov, A. N. & Pfleiderer, C. Spontaneous skyrmion ground states in magnetic metals. *Nature* **442**, 797–801 (2006).
6. Mühlbauer, S. et al. Skyrmion lattice in a chiral magnet. *Science* **323**, 915–919 (2009).
7. Nahas, Y. et al. Discovery of stable skyrmionic states in ferroelectric nanocomposites. *Nat. Commun.* **6**, 8542 (2015).
8. Zhang, Q. et al. Nanoscale bubble domains and topological transitions in ultrathin ferroelectric films. *Adv. Mater.* **29**, 1702375 (2017).
9. Gregg, J. M. Exotic domain states in ferroelectrics: searching for vortices and skyrmions. *Ferroelectrics* **433**, 74–87 (2012).
10. Naumov, I. I., Bellaiche, L. & Fu, H. Unusual phase transitions in ferroelectric nanodisks and nanorods. *Nature* **432**, 737–740 (2004).
11. Salahuddin, S. & Datta, S. Use of negative capacitance to provide voltage amplification for low power nanoscale devices. *Nano Lett.* **8**, 405–410 (2008).
12. Salahuddin, S. & Datta, S. Can the subthreshold swing in a classical FET be lowered below 60 mV/decade? In *2008 IEEE International Electron Devices Meeting* 1–4 (IEEE, 2008).
13. Theis, T. N. & Solomon, P. M. It's time to reinvent the transistor! *Science* **327**, 1600–1601 (2010).
14. Zubko, P. et al. Negative capacitance in multidomain ferroelectric superlattices. *Nature* **534**, 524–528 (2016).
15. Appleby, D. J. R. et al. Experimental observation of negative capacitance in ferroelectrics at room temperature. *Nano Lett.* **14**, 3864–3868 (2014).
16. Íñiguez, J., Zubko, P., Luk'yanchuk, I. & Cano, A. Ferroelectric negative capacitance. *Nat. Rev. Mater.* **4**, 243–256 (2019).
17. Hoffman, M. et al. Unveiling the double-well energy landscape in a ferroelectric layer. *Nature* **565**, 464–467 (2019).
18. Bratkovsky, A. M. & Levanyuk, A. P. Depolarizing field and "real" hysteresis loops in nanometer-scale ferroelectric films. *Appl. Phys. Lett.* **89**, 253108 (2006).
19. Wang, X. et al. Van der Waals negative capacitance transistors. *Nat. Commun.* **10**, 3037 (2019).
20. Lines, M. E. & Glass, A. M. *Principles and Applications of Ferroelectrics and Related Materials* (Clarendon Press, 1977).
21. Wu, X., Yang, E. S. & Evans, H. L. Negative capacitance at metal-semiconductor interfaces. *J. Appl. Phys.* **68**, 2845–2848 (1990).
22. Hoffman, M. et al. Ferroelectric negative capacitance domain dynamics. *J. Appl. Phys.* **123**, 184101 (2018).
23. Damodaran, A. R. et al. Large polarization gradients and temperature-stable responses in compositionally-graded ferroelectrics. *Nat. Commun.* **8**, 14961 (2017).
24. O'Neill, D., Bowman, R. M. & Gregg, J. M. Dielectric enhancement and Maxwell–Wagner effects in ferroelectric superlattice structures. *Appl. Phys. Lett.* **77**, 1520–1522 (2000).
25. Catalan, G., O'Neill, D., Bowman, R. M. & Gregg, J. M. Relaxor features in ferroelectric superlattices: a Maxwell–Wagner approach. *Appl. Phys. Lett.* **77**, 3078–3080 (2000).
26. Arai, H. et al. Fundamental characteristics of superconducting fault current limiter using LC resonance circuit. *IEEE Trans. Appl. Supercond.* **16**, 642–645 (2006).
27. Luk'yanchuk, I. et al. Electrodynamics of ferroelectric films with negative capacitance. *Phys. Rev. B* **98**, 024107 (2018).
28. Kamba, S. et al. Dielectric dispersion of the relaxor PLZT ceramics in the frequency range 20 Hz-100 THz. *J. Phys. Condens. Matter* **12**, 497–519 (2000).
29. Bovtun, V. et al. Comparison of the dielectric response of relaxor $PbMg_{1/3}Nb_{2/3}O_3$ ceramics and single crystals. *Integr. Ferroelectr.* **69**, 3–10 (2005).
30. Kittel, C.*Introduction to Solid State Physics* (Wiley, 1966).
31. Watanabe, Y. in *Ferroelectric Thin Films: Basic Properties and Device Physics for Memory Applications* (eds Okuyama, M. & Ishibashi, Y.) 177–199 (Springer, 2005).
32. Zubko, P., Stucki, N., Lichtensteiger, C. & Triscone, J.-M. X-ray diffraction studies of 180° ferroelectric domains in $PbTiO_3$/$SrTiO_3$ superlattices under an applied electric field. *Phys. Rev. Lett.* **104**, 187601 (2010).
33. Boulle, A., Infante & Lemée, N. Diffuse X-ray scattering from 180° ferroelectric stripe domains: polarization-induced strain, period disorder and wall roughness. *J. Appl. Cryst.* **49**, 845–855 (2016).
34. Okamura et al. Transition to and from the skyrmion lattice phase by electric fields in a magnetoelectric compound. *Nat. Commun.* **7**, 12669 (2016).
35. Fujishiro et al. Topological transitions among skyrmion- and hedgehog-lattice states in cubic chiral magnets. *Nat. Commun.* **10**, 1059 (2019).
36. Yang et al. Electric field driven evolution of topological domain structure in hexagonal manganites. *Phys. Rev. B* **96**, 144103 (2017).
37. Zong et al. Evidence for topological defects in a photoinduced phase transition. *Nat. Phys.* **15**, 27–31 (2019).
38. Schulz, A. et al. Emergent electrodynamics of skyrmions in a chiral magnet. *Nat. Phys.* **8**, 301–304 (2012).

Methods

Sample preparation using RHEED-assisted pulsed laser deposition. $(SrTiO_3)_{16}/(PbTiO_3)_{16}/(SrTiO_3)_{16}$ trilayer and $[(PbTiO_3)_n/(SrTiO_3)_n]_m$ (n is the number of monolayers, $n=8$–16, m is the number of repeats of the stacking sequence, $m=3$–8) superlattices were sandwiched between a 10 nm $SrRuO_3$ electrode at the bottom and 60 nm $SrRuO_3$ electrode at the top. The trilayer and superlattices were synthesized on TiO_2-terminated single-crystalline $SrTiO_3$ (001) substrates by RHEED-assisted pulsed laser deposition (KrF laser). The $PbTiO_3$ and $SrTiO_3$ layers were grown at 600 °C under 100 mtorr oxygen pressure. The growth temperature and oxygen pressure for the bottom $SrRuO_3$ layer were 700 °C and 50 mtorr, respectively, and for the top $SrRuO_3$ layer the corresponding parameters were 600 °C and 100 mtorr. For all materials, the laser fluence was 1.5 J cm^{-2} with a repetition rate of 10 Hz. RHEED was used during the deposition to ensure the maintenance of a layer-by-layer growth mode for both $PbTiO_3$ and $SrTiO_3$. The specular RHEED spot was used to monitor the RHEED oscillations. After deposition, the superlattices were annealed for 10 min under 50 torr oxygen pressure to promote full oxidation and then cooled to room temperature under the same oxygen pressure.

Structural analysis. *Laboratory-based X-ray diffraction.* The structures of the trilayer and superlattices were characterized using a Panalytical X'Pert Pro X-ray diffractometer with Cu Kα radiation ($\lambda=1.5405$ Å). The high crystallinity of the films and smooth nature of the interfaces were confirmed by θ–2θ symmetric X-ray diffraction scans around the (002) reflection, which showed strong superlattice peaks and Laue oscillations (not shown).

Synchrotron X-ray diffraction. To obtain a comprehensive picture of the structures of the skyrmions in the trilayers and superlattices as well as information on the in-plane and out-of-plane ordering and temperature-dependent skyrmion structures, further structural characterization was performed using synchrotron-based X-ray diffraction with monochromatic hard X-ray beams of 10–25 keV at the 33-BM-C, 33-ID-B, 7-ID-C and 12-ID-B beamlines of the Advanced Photon Source (APS), Argonne National Laboratory. The Huber and Newport diffractometers used at APS allowed us to determine the orientation of our crystals reliably, and to obtain 3D reciprocal space mappings based on rocking scan sampling with high angular accuracy. The high fluxes from the synchrotron X-ray source at these beamlines allowed the detection of the weak diffracted intensities arising from the lattice modulations associated with the polar skyrmion bubbles present in the $(PbTiO_3)_n/(SrTiO_3)_n$ superlattices.

Macroscopic capacitance measurements. *Out-of-plane measurements.* To measure the electrical properties of the superlattices, circular capacitor structures of 25, 50 and 100 μm diameters were fabricated using pulsed laser deposition followed by photolithography and etching. The fabrication involved three processes: 1) etching, 2) lift-off and 3) shadow mask deposition. First, photolithography was used to define the photoresist layer. Dry etching was carried out by argon ion beam milling at 1×10^{-4} torr argon pressure at a rate of 6 nm min^{-1} to remove the top electrode layer. Temperature-dependent small-signal a.c. permittivity was measured using an E4990A Impedance Analyzer with an a.c. excitation voltage of 10 mV at various frequencies.

In-plane measurements. A transmission-line approach was used to measure the in-plane dielectric properties of the $[(PbTiO_3)_{16}/(SrTiO_3)_{16}]_8$ superlattice at microwave frequencies ranging from 100 MHz to 10 GHz. To perform these measurements, an array of eight gold co-planar waveguide (CPW) transmission lines ranging in length from 0.42 to 6.60 mm were patterned on the surface of the superlattice film using standard lift-off fabrication techniques (Extended Data Fig. 6a). The central conductor of the CPWs had a width of 20 μm and was separated from 150 μm ground planes by a width of 5 μm. An identical pattern was also fabricated on a bare $SrTiO_3$ (001) substrate for reference. The dimensions of the devices were measured using optical microscopy and profilometry, and the conductivity of the gold was obtained from d.c. resistance measurements.

The scattering (S-) parameters of the transmission line devices were then measured at room temperature from 100 MHz to 10 GHz using a vector network analyser at a power of −15 dBm and an IR bandwidth of 30 Hz. The vector network analyser was calibrated using custom-fabricated on-wafer calibration standards with device geometries consistent with the devices patterned on the superlattice film and bare substrate. The National Institute of Standards and Technology (NIST) StatistiCal software package was used to implement the multiline-TRL algorithm[39,40] to extract accurate estimates of the propagation constant (γ) from the S-parameter measurements of the CPWs on the superlattice films and bare substrate. The propagation constant is related to the distributed circuit parameters of the CPW by the relationship $\gamma=\sqrt{R+i\omega L}\sqrt{G+i\omega C}$, where R, L, G and C are the distributed resistance, inductance, conductance and capacitance per unit length, respectively, and ω is the angular frequency. These circuit parameters are related to the geometries and material properties of the metal layers comprising the CPW and the surrounding dielectric layers, which were probed by electric fields generated in the devices during measurement (Extended Data Fig. 6b). If R and L are known, C and G, which are proportional to the real and imaginary parts of the effective permittivity, respectively, can be extracted from γ. In the devices on the superlattice film chip, the in-plane electric fields interact with both the superlattice film and the substrate, therefore some portion of the overall measured C and G can be attributed to the permittivity of the film (C_{FILM}, G_{FILM}) and to the permittivity of the substrate (C_{SUB}, G_{SUB}), as illustrated in the stylized circuit model for these transmission lines (Extended Data Fig. 6c). The measurements on the bare substrate were used to aid separating these contributions to the overall measurement. Finite element simulations of the device structures incorporating the measured dimensions and metal properties were generated and validated by comparison with known devices. These simulations were first used to obtain the R and L values for the CPW devices in order to extract C and G, and finally were used to obtain the mapping function relating C and G to the real (ε') and imaginary (ε'') parts of the permittivity, respectively.

In situ electric field-dependent structural measurements. Synchrotron X-ray diffraction measurements as a function of electric field (applied voltage divided by the thickness of the sample) were conducted at the 7-ID-C, 32-ID-B and 12-ID-B beamlines at APS using $(PbTiO_3)_n/(SrTiO_3)_n$ superlattice samples ($n=16$, 20, total superlattice thickness of ~100 nm) deposited on $SrTiO_3$ (100) substrates. By employing a capacitor device geometry with the superlattice sandwiched between $SrRuO_3$ electrodes grown at the substrate interface and on top of the superlattice stack, additional in situ electric field-dependent measurements of the superlattices were performed at the 7-ID-C and 32-ID-B beamlines. For the first device geometry used at the 32-ID-B beamline, the incident X-ray beam of 10 keV was focused using two Kirkpatrick–Baez mirrors to a spot of ~30 μm × 90 μm on the top electrode of the capacitor device with a lateral size of 150 μm × 150 μm. To study the effect of the out-of-plane electric field, a constant d.c. voltage was applied to the capacitor device, and the intensities of various peaks were monitored with a gated area detector, which acquired the distribution of scattered X-ray intensity in reciprocal space, followed by reciprocal space mapping reconstruction. Device-to-device data reproducibility was additionally checked at the 7-ID-C beamline using several capacitor devices with a diameter of 25 μm and an 11 keV X-ray beam focused by a zone plate to ~1 μm × 1 μm on the top of the capacitors. For these smaller capacitors, application of the electric field was initiated using a sharp platinum tip of a few nanometres in size placed in contact with the top electrode under a nanoscale probe imaging station called an X-ray scanning near-field optical microscope[41].

Phase-field modelling. To predict and understand the structures and responses of the polar skyrmions under applied electric and thermal stimuli, phase-field simulations[42,43] were performed for the $(PbTiO_3)_{16}/(SrTiO_3)_{16}$ superlattice on a $SrTiO_3$ substrate by evolving spatial distributions of the polarization vector (**P**), strain and electric potential (and thus electric field)[1,2,43]:

$$\frac{\partial P_i}{\partial t}=-L\frac{\delta F}{\delta P_i}(i=1,3) \qquad (1)$$

where t is the simulation time step, L is the kinetic coefficient related to the bulk domain wall mobility and F is the total free energy of the superlattice.

The total free energy (F) contains contributions from mechanical, electrostatic, Landau chemical and polarization gradient energies:

$$F=\int_V\left(f_{\text{mech}}+f_{\text{elec}}+f_{\text{Land}}+f_{\text{grad}}\right)\mathrm{d}V \qquad (2)$$

Detailed expressions of the energy densities and material parameters can be found elsewhere[44,45]. The simulation cell was discretized into 3D grids of $200\times200\times350$, with each grid representing 0.4 nm. Periodic boundary conditions were applied along the in-plane dimensions while a superposition scheme[44] was imposed along the thickness dimension, which was composed of 30 grids of substrate, 288 grids of thin-film layers (which consist of repeating units of 16 $PbTiO_3$ layers and 16 $SrTiO_3$ layers) and 32 grids of vacuum. The thin-film boundary condition was applied where it was stress-free on the top of the film and the displacement was zero on the bottom of the substrate sufficiently far away from the substrate/thin-film interface[43]. An iteration perturbation method was used to account for the elastic inhomogeneity of the two materials[45].

The local electric potential (φ) can be obtained by solving Poisson's equation:[44] $\varepsilon_0K_{ij}\frac{\partial^2\varphi}{\partial x_ix_j}=P_{i,i}$, where ε_0 is the permittivity of a vacuum and K_{ij} is the background dielectric constant[42]. The electric field (E_i) can be expressed by the gradient of the electric potential, that is, $E_i=-\nabla_i\varphi$. A close-circuit electric boundary condition[46] was used with the electric potential both at the bottom and top of the thin film set to zero or a specified applied potential. The polar skyrmion array[1] was stabilized at room temperature, starting from the initial random noise, which was used for the follow-up calculations. The macroscopic dielectric constant at a given electric potential bias was calculated by giving small potential perturbations according to $\varepsilon_{33}=\frac{\Delta<P_3>d}{\varepsilon_0\Delta\phi}+K_{33}$, where d is the thickness of the thin film. The spatially resolved local permittivity[3] is defined as $\varepsilon_{33}=\frac{\Delta P_3}{\varepsilon_0\Delta E_3}+K_{33}$. The thermal stability of the polar skyrmion was also investigated in the temperature range 300–800 K. Because $PbTiO_3$ and $SrTiO_3$ have similar thermal expansion coefficients, the substrate strain was assumed to be constant across the whole temperature range.

The lower bound of the transition temperature was estimated by adding a 0.05% relaxation of the substrate strain (which is the uncertainty of the measurement). The switching kinetics were also studied with an applied field in the range −1,500 to +1,500 kV cm^{-1}.

Second-principles calculations. The second-principles calculations were performed using the same methodology presented in previous works[1,47–49] as implemented in the SCALE-UP package[47]. The interactions inside the $PbTiO_3$ or $SrTiO_3$ layers can be described using the potentials for the bulk materials[48]. These potentials give qualitatively correct descriptions of the lattice dynamical properties and structural phase transitions of both materials. Then, we treated the interactions at the interface between $PbTiO_3$ and $SrTiO_3$ assuming a simple numerical average for the interactions of the ions pairs touching or crossing the interface. The main effect of the stacking is electrostatic, wherein long-range dipole–dipole interactions are governed by a bare electronic dielectric constant (ϵ_∞), which is taken as a weighted average of the first-principles results for bulk $PbTiO_3$ ($8.5\epsilon_0$) and $SrTiO_3$ ($6.2\epsilon_0$) with the weights reflecting the composition of the superlattice. To preserve the electrostatic energy within each material as close as possible to the bulk parent compounds, the Born effective charge tensors of the inner atoms were rescaled by $\sqrt{\epsilon_\infty}/\epsilon_\infty^{ABO_3}$ (where ABO_3 represents $PbTiO_3$ or $SrTiO_3$ depending on the layer).

The second-principles parameters of both materials were fitted from density functional theory imposing a hydrostatic pressure of −11.2 GPa to counter the underestimation of the local density approximation of the cubic lattice constant that was taken as the reference structure. We imposed an epitaxial constraint assuming in-plane lattice constants of $a=b=3.901$ Å, forming an angle $\gamma=90°$, which corresponds to a $SrTiO_3$ (001)-oriented substrate.

Following this strategy, we were able to construct models for the superlattices with arbitrary n stacking. For the simulations, we used periodically repeated supercells containing 20×20 elemental perovskite units in-plane, and one full superlattice period in the out-of-plane direction. To solve the models, we used standard Monte-Carlo and Langevin molecular dynamics methods; at low temperature, only random configurations along the Markov chains that produce a lowering in the energy are accepted. By following this procedure as an equivalent to structural relaxations we found the ground state. The local polarizations were obtained within a linear approximation, computing the product of the atomic displacements from the reference structure, which correspond to the ideal cubic perovskite, times the Born effective charge tensor divided by the volume of the unit cell. The skyrmion number (N_{SK}) was obtained from the local dipoles computing the normalized polarization field defined along each slice of in-plane $20\times20\times1$ elemental perovskite units of our supercell and solving Equation (1), obtaining a skyrmion number that corresponds to an integer number[1,50].

Finally, the local dielectric constant and the electric susceptibilities were computed following the strategy presented in ref. [2]. There, the inverse of the dielectric constant was defined to be a measure of the change in the local electric field with the variation of the electrical boundary conditions that sets the macroscale electric displacement vector. The normal component of the displacement electric field can be monitored by the external electric field. In the same spirit, the local electric susceptibilities measure the changes in the local polarization under the application of the same external electric field.

To compute the global dielectric permittivity, the skyrmion structure was relaxed under different external electric fields of increasing magnitude. The starting configuration for a given value of the external field was the relaxed structure obtained for the former field. After relaxation, the global polarization along the z direction was averaged for the whole supercell. From the plot of P_z versus the external field, a fit to a Landau-type equation of state was performed, including up to five order terms. Finally, the global electronic susceptibility was estimated as $\epsilon_z = 1 + \frac{1}{\epsilon_0}\frac{\partial P_z}{\partial E_{ext,z}}$.

SCBED for local potential energy measurement. SCBED experiments were performed using an EMPAD in 4D-STEM and a transmission electron microscope operated at 300 keV with a beam current of 15 pA, semiconvergence angle of 2.0 mrad and a probe full-width at half-maximum of ~8 Å. The CBED patterns were captured by the EMPAD with the exposure time set to 1 ms per frame. The TEM specimen had a thickness of ~25 nm, as determined by CBED simulations using EMPAD. Cross-sectional measurements enabled access to the cross-section of the Bloch and Neél components of the skyrmions away from the interfaces, where the technique is most robust.

Both the ferroelectric polarization and electric field need to be measured independently and simultaneously to extract the local potential energy. First, long-range electric fields can be reconstructed from the deflection of the entire CBED pattern by the Lorentz force[29,30]. For this study, we focused on the deflection of the (000) beam as there are fewer polarity effects. Second, due to dynamical diffraction effects, the polarization direction can be retrieved from the diffraction intensity differences of Friedel pairs, such as (100)/($\bar{1}$00) and (001)/(00$\bar{1}$) for the x and z components of polarity, respectively. We carefully selected local regions with minimal tilt and thickness variations, as these effects complicate the analysis and give rise to non-trivial artefacts.

Once the electric and polarization fields had been measured, we could calculate the local potential energy of the system following the approach given in ref. [2].

Based on the analysis (Fig. 3), the potential energy has local maxima at the skyrmion domain walls, where the out-of-plane polarization (z component) is suppressed.

Probing the transient capacitance state. We applied a series of two identical, consecutive (U_1 and U_2 in Fig. 4a) unipolar pulses, with a pulse width of 10 µs, to the sample. Each pulse generated a field of 1,300 kV cm^{-1} in the film. During each pulse we monitored the current through the sample. The time delay between pulses was variable, given by t_d. During the time delay, no electric field was applied and the system began to relax to the ground (skyrmion) state. U_2 probes the capacitance at the time of application, and as such by varying t_d and comparing the currents I_1 and I_2 generated in the circuit in response to the pulses U_1 and U_2, we could probe the evolution of the sample back to the ground state. Upon subtracting the response (that is, I_2) to pulse U_2 from the response (that is, I_1) to pulse U_1, we observed a discernible difference between the response to the poling pulse (U_1) and the following pulse (U_2; Fig. 4). This difference is attributed to the formation of a transient capacitive state in which the system is driven out of equilibrium (toward the uniform polarization state) and then relaxes back to the ground state. The difference in response between U_1 and U_2 is largest for short delay times t_d and decays with longer delay times, as is expected while the transient state decays. This difference can be attributed to back-switching of the small remnant polarization of the sample; however, a similar experiment that includes a preset down pulse revealed that this cannot be the case (Fig. 5).

Data availability

All data supporting the findings of this study are available within the paper and/or are available from the authors upon reasonable request.

References

39. Marks, R. B. A multiline method of network analyzer calibration. *IEEE Trans. Microw. Theory Tech.* **39**, 1205–1215 (1991).
40. Williams, D. F., Wang, J. C. M. & Arz, U. An optimal vector-network analyzer calibration algorithm. *IEEE Trans. Microw. Theory Tech.* **51**, 2391–2401 (2003).
41. Li, Q. et al. Simultaneous scanning near-field optical and X-ray diffraction microscopy for correlative nanoscale structure–property characterization. *J. Synchrotron Radiat.* **26**, 1790–1796 (2019).
42. Towns, J. et al. XSEDE: accelerating scientific discovery. *Comput. Sci. Eng.* **16**, 62–74 (2014).
43. Nystrom, N. A., Levine, M. J., Roskies, R. Z. & Scott, J. R. Bridges: a uniquely flexible HPC resource for new communities and data analytics. In *Proc. 2015 XSEDE Conference: Scientific Advancements Enabled by Enhanced Cyberinfrastructure* Vol. 30, 1–8 (2015).
44. Chen, L.-Q. Phase-field method of phase transitions/domain structures in ferroelectric thin films: a review. *Appl. Phys. Lett.* **91**, 1835–1844 (2008).
45. Sheng, G., Li, Y. L. & Zhang, J. X. A modified Landau–Devonshire thermodynamic potential for strontium titanate. *Appl. Phys. Lett.* **96**, 232902 (2010).
46. Tagantsev, A. et al. Landau expansion for ferroelectrics: which variable to use? *Ferroelectrics* **375**, 19–27 (2008).
47. Wojdeł, J. C., Hermet, P., Ljungberg, M. P., Ghosez, P. & Íñiguez, J. First-principles model potentials for lattice-dynamical studies: general methodology and example of application to ferroic perovskite oxides. *J. Phys. Condens. Matter* **25**, 305401 (2013).
48. Wojdeł, J. C. & Íñiguez, J. Ferroelectric transitions at ferroelectric domain walls found from first-principles. *Phys. Rev. Lett.* **112**, 247603 (2014).
49. Gonçalves, M. A. P. et al. Theoretical guidelines to create and tune electric skyrmion bubbles. *Sci. Adv.* **5**, eaau7023 (2019).
50. B. Berg, B. & Lüscher, M. Definition and statistical distributions of a topological number in the lattice O(3) σ-model. *Nucl. Phys. B.* **190**, 412–424 (1981).

Acknowledgements

This work was supported by the Quantum Materials program of the Office of Basic Energy Sciences, US Department of Energy (DE-AC02-05CH11231). M.A.P.G. and J.Í. were funded by the Luxembourg National Research Fund through the CORE program (Grant FNR/C15/MS/10458889 NEWALLS). J.W.F., V.A.S., H.W. and L.W.M. acknowledge support from the US Department of Energy, Office of Science, Office of Basic Energy Sciences (Award number DE-SC-0012375) for the development and study of ferroic heterostructures. The phase-field simulations at Penn State were supported as part of the Computational Materials Sciences Program funded by the US Department of Energy, Office of Science, Basic Energy Sciences (Award number DE-SC0020145) and the Extreme Science and Engineering Discovery Environment (XSEDE) cluster, which is supported by the National Science Foundation (Grant ACI-1548562), and specifically, it used the Bridges system, which is supported by the NSF (Award number ACI-1445606)

at the Pittsburgh Supercomputing Center (PSC), under allocation DMR170006. F.G.O., P.G.F. and J.J. acknowledge financial support from the Spanish Ministry of Economy and Competitiveness (Grants FIS2015-64886-C5-2-P and PGC2018-096955-B-C41), and P.G.F. acknowledges support from Ramón y Cajal Foundation (Grant RyC-2013-12515). V.A.S., M.R.M., S.D., H.W., Z.Z., J.W.F. and H.Z. acknowledge use of the Advanced Photon Source, a US Department of Energy, Office of Science User Facility operated for the DOE Office of Science by Argonne National Laboratory under contract no. DE-AC02-06CH11357. V.A.S. and H.W. thank Q. Li and S. Marks for kind assistance in operating the XNOM station at the 7-ID-C beamline of APS. Y.T.S. and D.A.M. acknowledge support from the AFOSR Hybrid Materials MURI (Award number FA9550-18-1-0480). We acknowledge the electron microscopy facility of the National Science Foundation (Award numbers DMR-1719875 and DMR-1429155). E.J.M., C.J.L. and N.D.O. acknowledge J. C. Booth for establishing the high-frequency testing facility at NIST, funding E.J.M. and developing the original on-wafer techniques.

Author contributions

S.D. and R.R. designed the experiments. S.D. synthesized and characterized the trilayer and superlattice samples. S.D. facbricated the devices and S.D. and S. Saremi performed all macroscopic electrical measurements. Y.T.S. performed EMPAD characterization of the samples under the supervision of D.A.M. M.A.P.G., F.G.O., P.G.F., J.Í. and J.J. performed the second-principles calculations. Z.H. performed and analysed the phase-field calculations of the samples. V.A.S., M.R.M. and S.D. carried out the reciprocal space map studies of these samples using laboratory X-ray diffraction and synchrotron X-ray diffraction. V.A.S. carried out the electric field-dependent reciprocal space map studies of these samples using synchrotron X-ray diffraction. E.P. and S.D. performed electric field-dependent pulse dynamics studies. E.J.M. designed the layout, fabricated the in-plane devices and performed the microwave measurements, analysed the data and wrote the microwave section. N.D.O. and A.M.H. supervised the microwave research and N.D.O. wrote the algorithms that calibrated and processed the data, and wrote the analysis tools. C.J.L. wrote the algorithms that generated the layout, optimized the device performances and calibrated and processed the data. S.D., Z.H., V.A.S., J.J., L.Q.C. and R.R. analysed the data and co-wrote the manuscript. R.R., L.Q.C., L.W.M., S. Salahuddin and J.J. supervised the research. All authors contributed to the discussion and manuscript preparation.

Competing interests

The authors declare no competing financial interests.

Additional information

Extended data is available for this paper at https://doi.org/10.1038/s41563-020-00818-y.

Supplementary information is available for this paper at https://doi.org/10.1038/s41563-020-00818-y.

Correspondence and requests for materials should be addressed to S.D. or R.R.

Reprints and permissions information is available at www.nature.com/reprints.

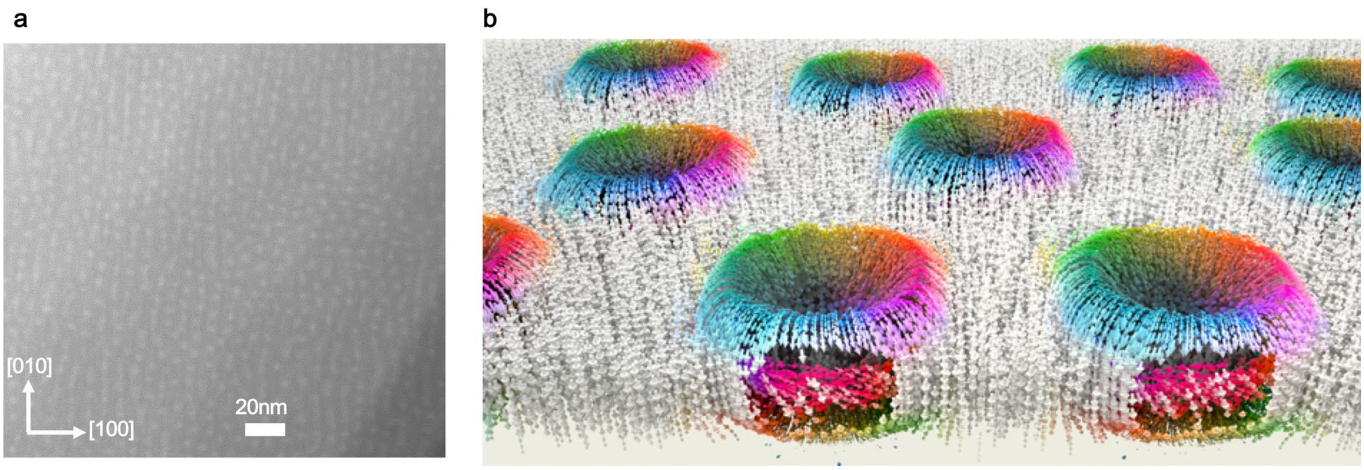

Extended Data Fig. 1 | Polar skyrmion structure in $[(SrTiO_3)_{16}/(PbTiO_3)_{16}]_8$ superlattice. a, Planar-view dark-field STEM imaging shows the widespread occurrence of nanometer-size (~8 nm) skyrmion formation along the [100] and [010] directions. **b**, Second-principles calculations of the skyrmion structure in the superlattice. The hedgehog-like skyrmion (Topological number +1) at the top and bottom interface between $SrTiO_3$ and $PbTiO_3$, and the Bloch-like skyrmion (topological number +1) at the central plane in $PbTiO_3$ are clearly visible. The arrows represent the normalized electric dipole moments.

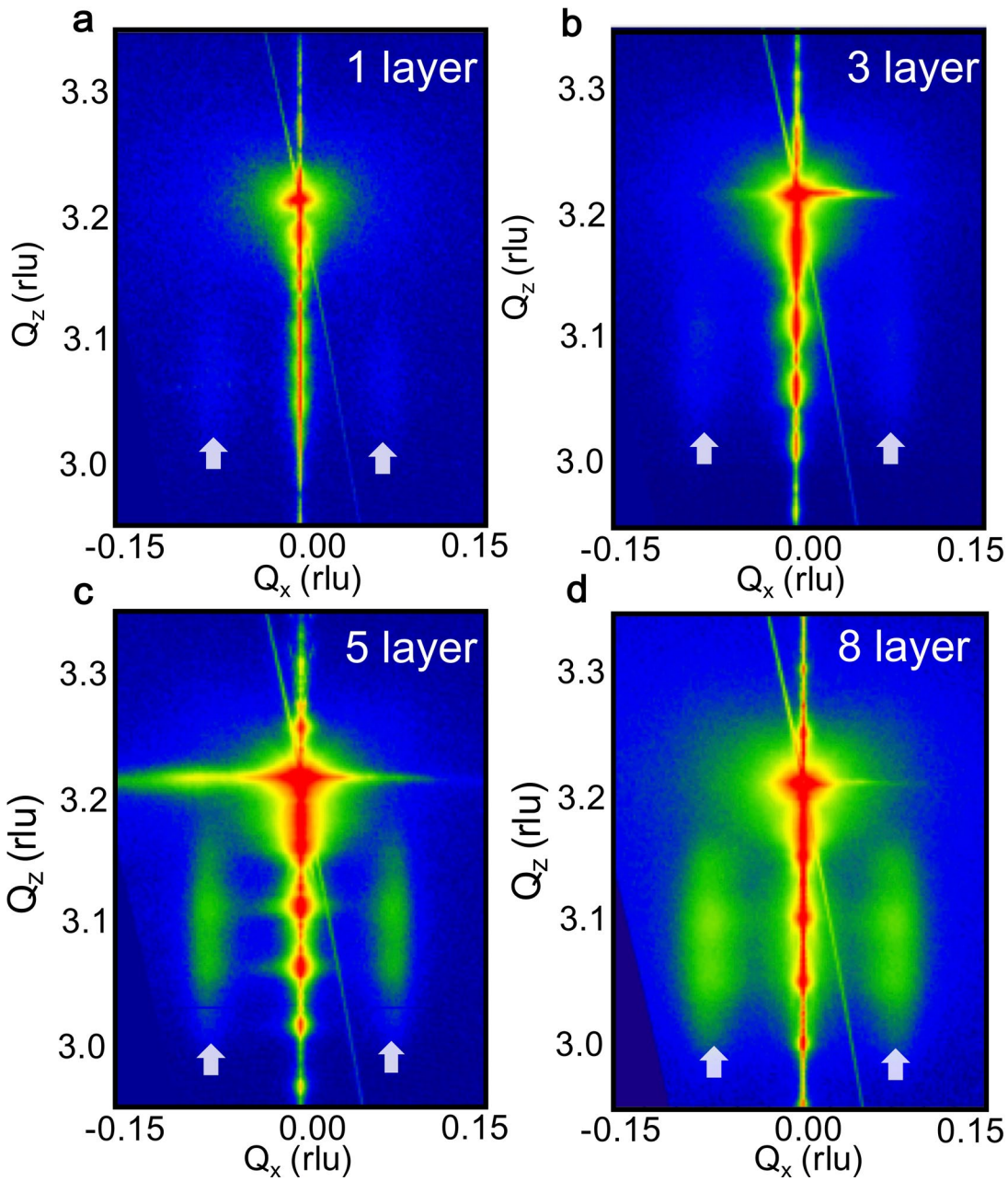

Extended Data Fig. 2 | Synchrotron-based symmetric three-dimensional reciprocal space mapping about the (002) diffraction condition of the $SrTiO_3$ substrate. Reciprocal space mapping of **a**, $(SrTiO_3)_{16}/(PbTiO_3)_{16}/(SrTiO_3)_{16}$ trilayer, **b**, $[(PbTiO_3)_{16}/(SrTiO_3)_{16}]_3$ superlattice, **c**, $[(PbTiO_3)_{16}/(SrTiO_3)_{16}]_5$ superlattice and **d**, $[(PbTiO_3)_{16}/(SrTiO_3)_{16}]_8$ superlattice. The satellite peaks along (100) direction (side-lobes; white arrow) which correspond to the skyrmions.

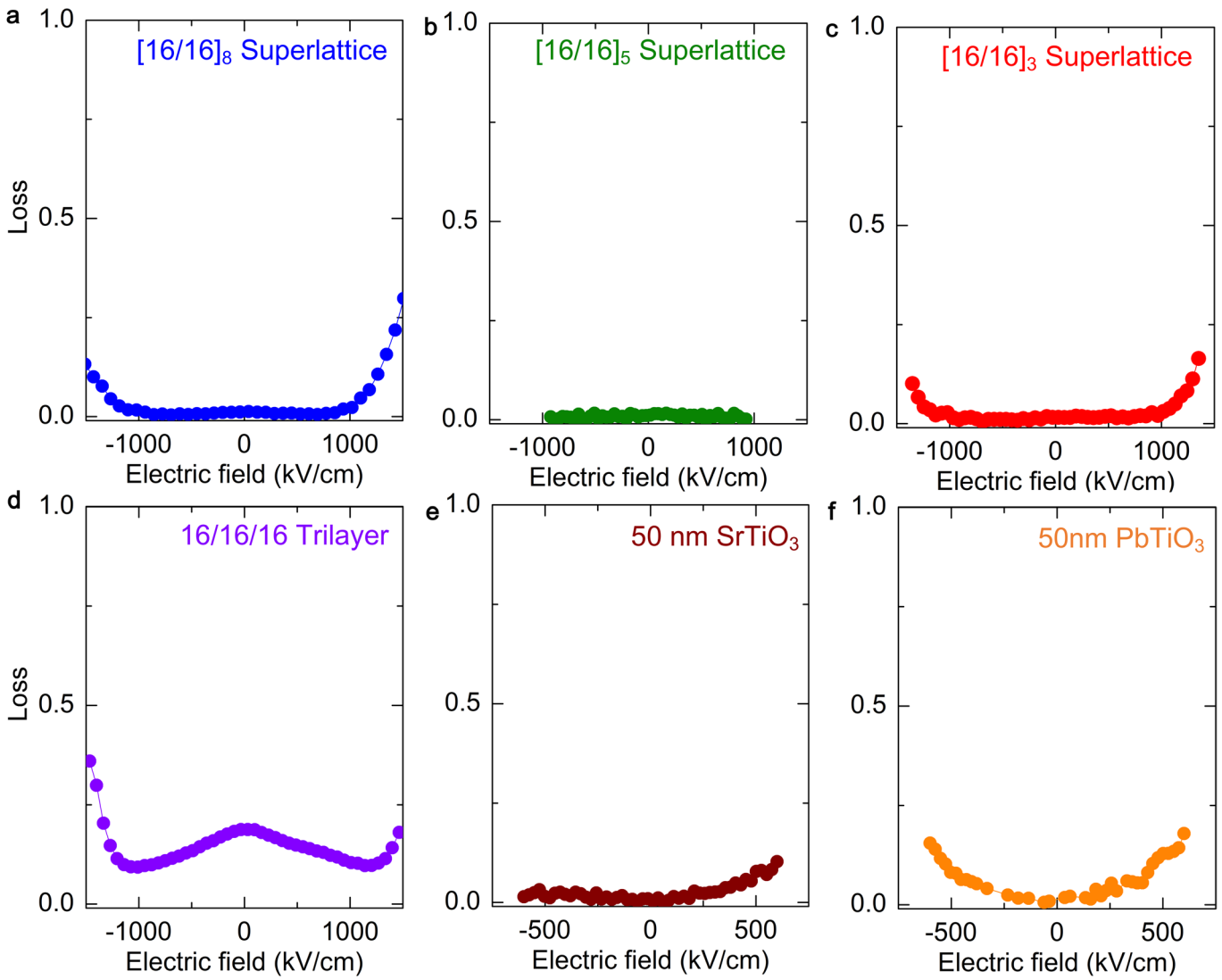

Extended Data Fig. 3 | Loss Tangent as a function of electric field. The loss tangent (tanδ) as a function of electric field for **a**, $[(SrTiO_3)_{16}/(PbTiO_3)_{16}]_8$ superlattice, **b**, $[(SrTiO_3)_{16}/(PbTiO_3)_{16}]_5$ superlattice, **c**, $[(SrTiO_3)_{16}/(PbTiO_3)_{16}]_3$ superlattice, **d**, $(SrTiO_3)_{16}/(PbTiO_3)_{16}/(SrTiO_3)_{16}$ trilayer which is in the skyrmion state compared to its constituents **e**, 50nm $SrTiO_3$ (brown) and **f**, 50 nm-thick $PbTiO_3$ layer.

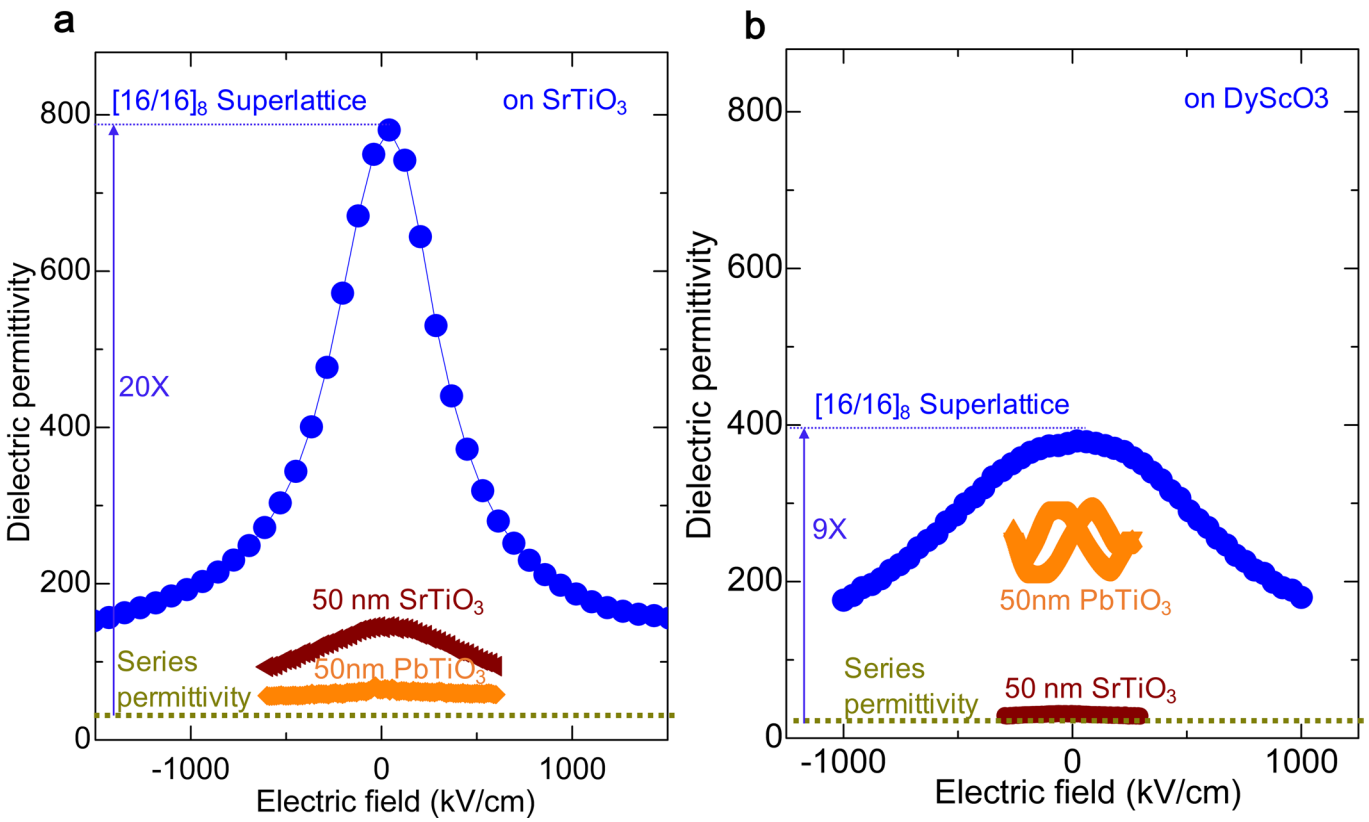

Extended Data Fig. 4 | Measured out-of-plane dielectric permittivity as a function of electric field for the. a, $[(SrTiO_3)_{16}/(PbTiO_3)_{16}]_8$ superlattice (skyrmion sample) compared with 50nm $SrTiO_3$ and 50 nm $PbTiO_3$ layers on $SrTiO_3$ (001) and **b**, $[(SrTiO_3)_{16}/(PbTiO_3)_{16}]_8$ superlattice (vortex sample) compared with 50nm $SrTiO_3$ and 50 nm $PbTiO_3$ layers on $DyScO_3$ (110) substrate. The enhancement of dielectric permittivity for the skyrmion sample ~ 20X larger compared to its series permittivity whereas it only ~ 9X for vortex samples.

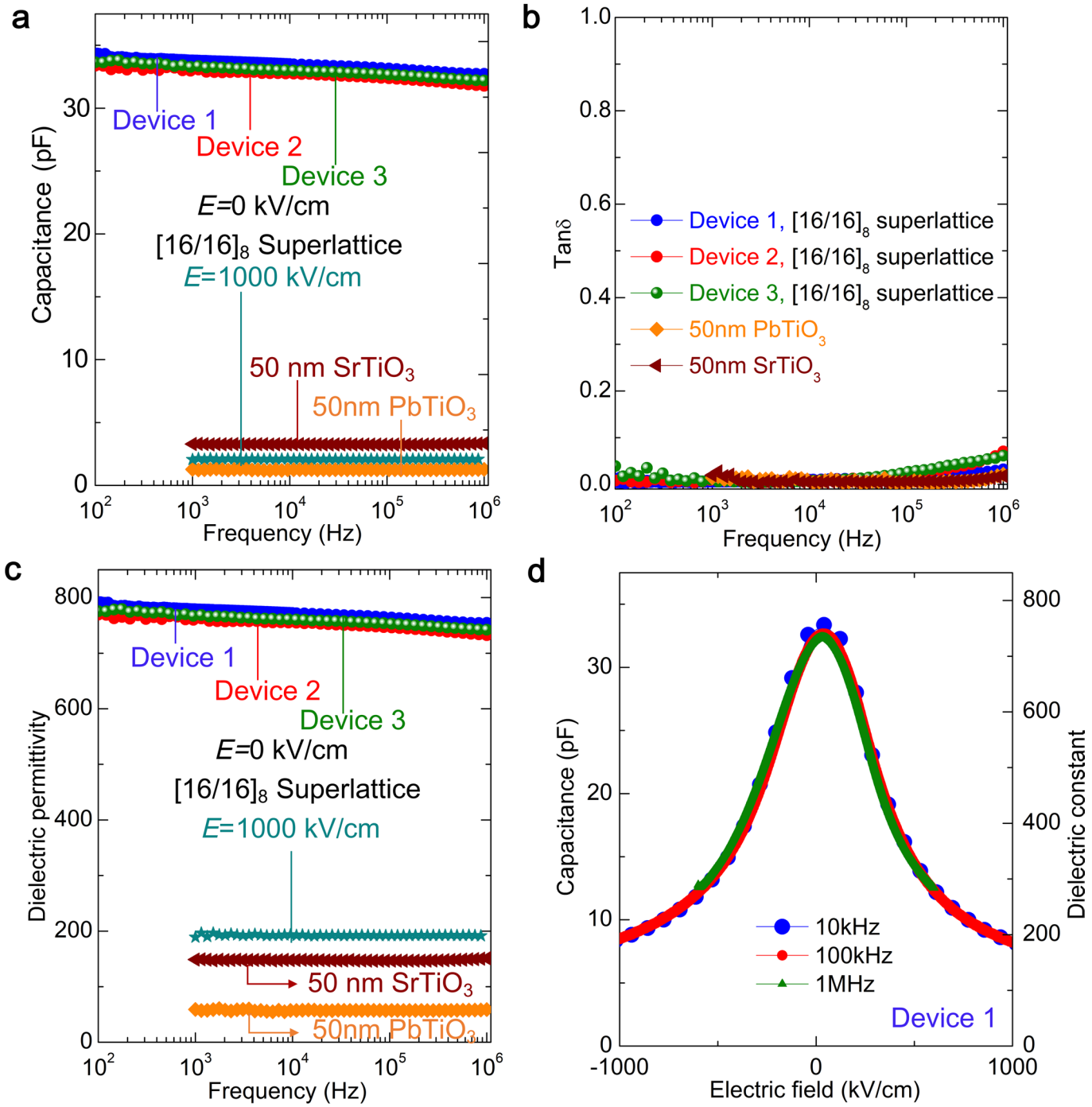

Extended Data Fig. 5 | Out-of-plane dielectric permittivity as a function of frequency measured on three different devices. a, Capacitance vs Frequency of $[(SrTiO_3)_{16}/(PbTiO_3)_{16}]_8$ superlattice (superlattice total thickness: 100nm, capacitor size of the measurement: 25μm) compared with 50nm $PbTiO_3$ (orange), 50nm $SrTiO_3$ layers (brown) (capacitor size of the measurement: 25 μm) at electric field E=0 kV/cm and E=1000 kV/cm (light green). **b**, Tangent loss (Tan δ) vs Frequency of $[(SrTiO_3)_{16}/(PbTiO_3)_{16}]_8$ superlattice compared with 50nm $PbTiO_3$ (orange) and 50nm $SrTiO_3$ (brown) layers. It shows the Tanδ which is approximately an order of magnitude smaller than for samples which show Maxwell-Wagner (MW) effects in the literature (Ref. [24,25]). **c**, Dielectric permittivity vs Frequency of $[(SrTiO_3)_{16}/(PbTiO_3)_{16}]_8$ superlattice which is in the skyrmion state measured in three different capacitor devices compared with 50nm $PbTiO_3$ (orange) and 50nm $SrTiO_3$ (brown) layers at electric field E=0 kV/cm and E=1000 kV/cm (light green). **d**, Capacitance (left axis), permittivity (right axis) as a function of electric field of $[(SrTiO_3)_{16}/(PbTiO_3)_{16}]_8$ superlattice which is in the skyrmion state at 10kHz (blue), 100kHz (red) and 1MHz (green). The capacitance and permittivity change by ~ 4% over the measured frequency range. This reveals that the calculated negative permittivity from this macroscopic measurement is independent of measured frequency in this range.

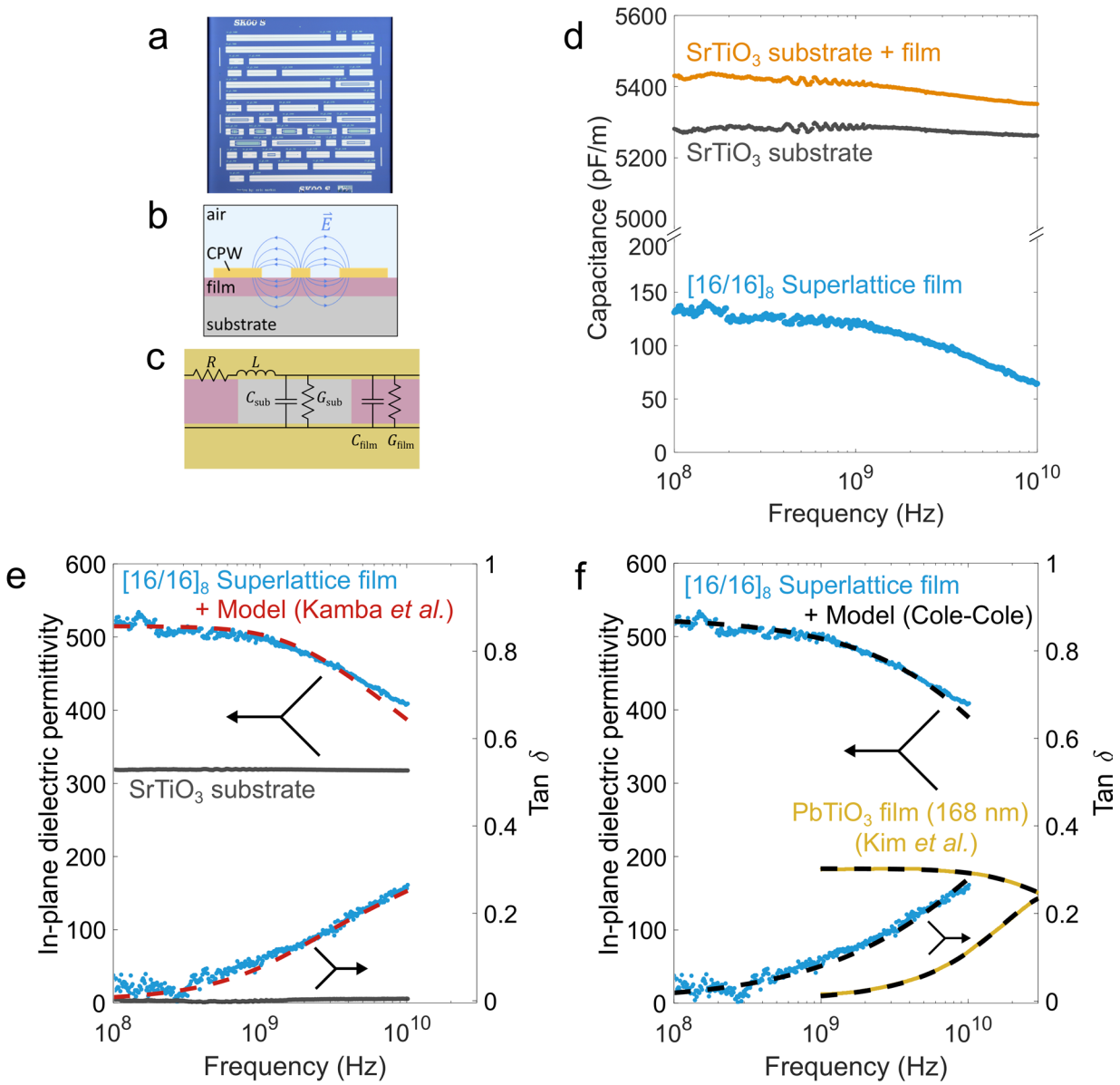

Extended Data Fig. 6 | In-plane dielectric permittivity of $[(SrTiO_3)_{16}/(PbTiO_3)_{16}]_8$ superlattice at microwave frequencies from 100 MHz to 10 GHz. **a**, A schematic of co-planar Waveguide (CPW) transmission lines for microwave-frequency permittivity characterization. **b**, A cross-sectional view of the CPW illustrating the electric fields between the center conductor and ground planes. **c**, A circuit model of the CPW transmission line showing how the total measured capacitance of the transmission line (C) is comprised of a portion related to the permittivity of the $SrTiO_3$ substrate (C_{SUB}), and a portion related to the permittivity of the superlattice (C_{FILM}). **d**, The measured capacitance of the CPW transmission lines on the superlattice (purple), and $SrTiO_3$ substrate (red) are shown. Finite element simulations and the measurements of the bare $SrTiO_3$ substrate are used to analyze and isolate the portion of the total capacitance which is related to the permittivity of the superlattice (blue). **e**, The real part of the in-plane dielectric permittivity (left-hand y-axis) and the loss tangent (right-hand y-axis) are determined from the capacitance and conductance measurements via a mapping function obtained from 2D finite element modeling of the CPW structures; **f**, Cole-Cole model of the in-plane complex permittivity of the superlattice from 100 MHz to 10 GHz (Supplementary Note 2).

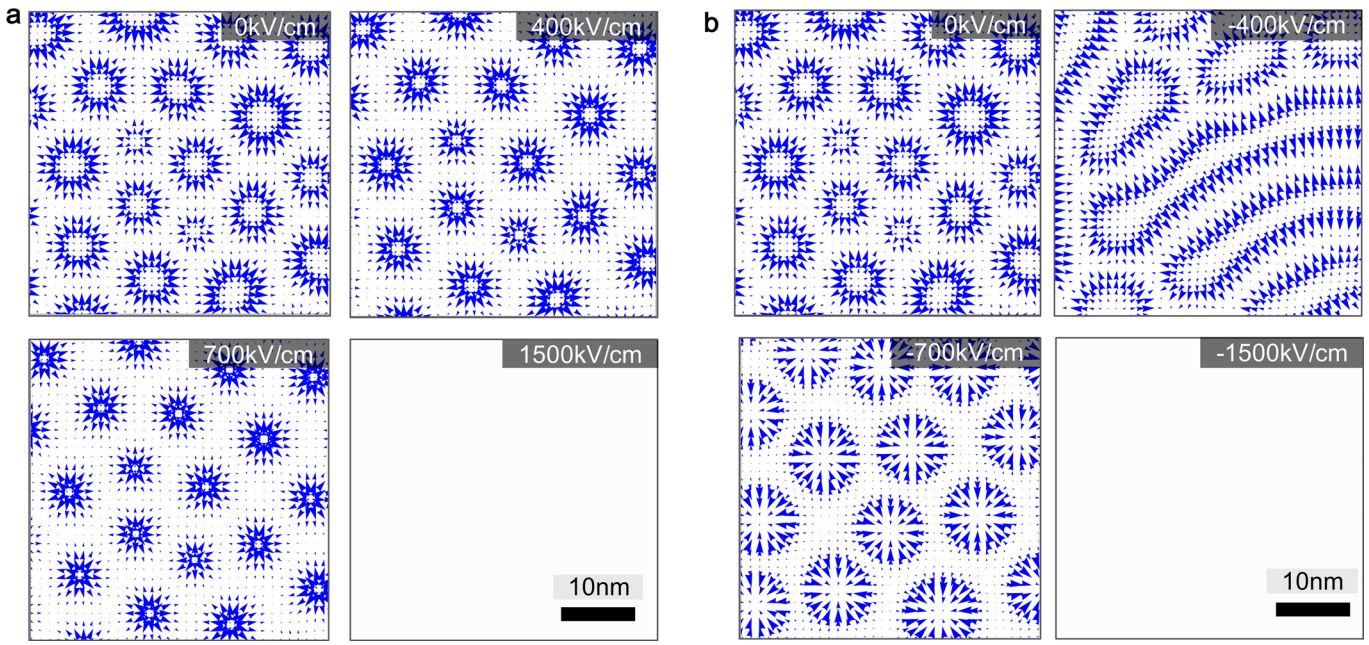

Extended Data Fig. 7 | Phase field simulation of the switching dynamics of skyrmions under different externally applied fields. The size of the skyrmion decreases progressively until all the skyrmions implode at ~1500 kV/cm. **a**, positive field. **b**, negative field.

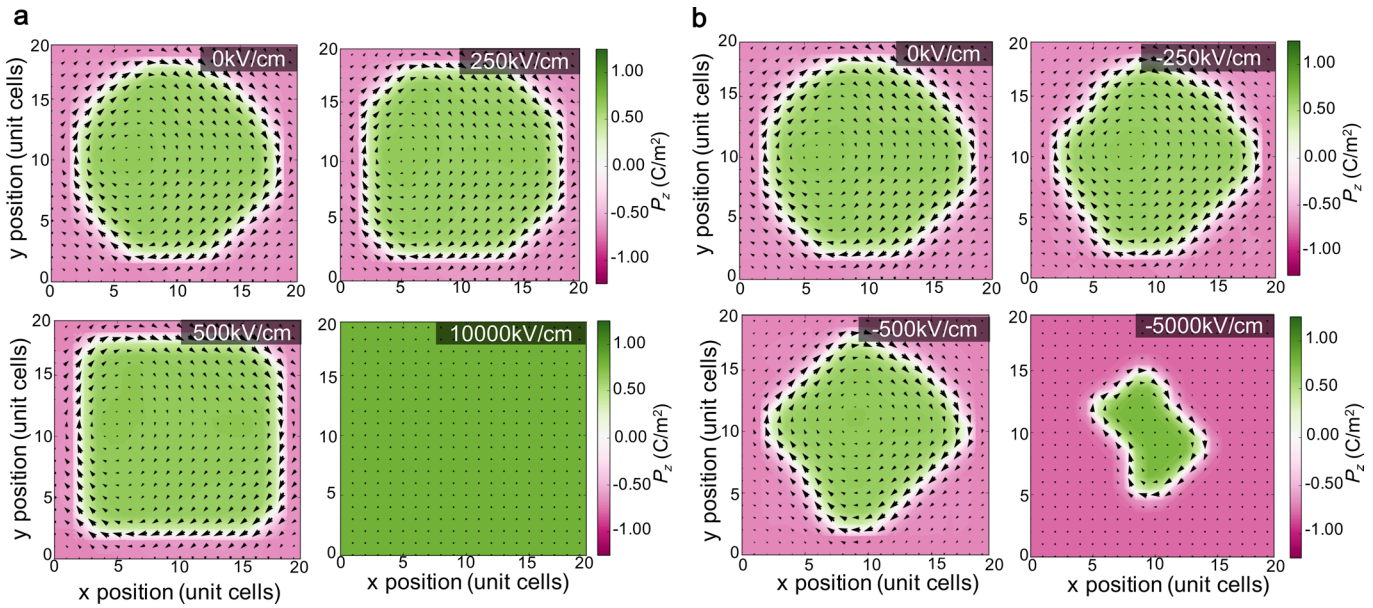

Extended Data Fig. 8 | Second principle simulation of the evolution of the local polarization texture at the central layer of the $PbTiO_3$ under different external fields. The arrows represent the polarization on the *x*-*y* plane, while the colors represent the component of the out-of-plane polarization as indicated in the legend. The snapshots correspond to Monte Carlo simulations at different electric fields, where the initial configuration for a new magnitude of the field was the relaxed structure from the previous field. **a**, positive field. **b**, negative field. For the sake of clarity let us assume that the core of the skyrmion has a polarization pointing along the +*z* direction, while it points down along −*z* at the periphery, at null external field. Let us assume also that we switch on an external field parallel to the polarization at the center of the skyrmion, as it is done in panel (a) (positive values of the field). Then, as it is clearly visible from the snapshots at 250 kV/cm and 500 kV/cm, the domain with a polarization parallel to the external field increases at the expenses of the other. The domain wall of the skyrmion has moved, but there will be always a domain wall between the core and the periphery of the skyrmion where the out-of-plane polarization vanishes (see the regions plotted in white delimiting the surface of the skyrmion). There is a tendency of the domain wall to polarize with the appearance of a Bloch component to minimize the energy (see the arrows within the white regions of the panels)[48]. This Bloch components of the polarization are perpendicular to the applied field and do not couple with it. Therefore, they will be always present, independently of the sizes of the domains up and down. These Bloch components closing a loop around the domain wall are precisely at the origin of the non-trivial topological textures (the vortex they form determine why the skyrmion number is +1). The larger the electric field, the larger the size of the domain that aligns with it (with the criterion chosen for this example, the skyrmion expands). For a critical field, this domain will cover all space and the transition to a monodomain state will be completed. Right before the transition, a singularity appears: the stereographic projection of our dipole patterns does not completely wrap the unit sphere. That is exactly the point where the skyrmion number changes from +1 (non-trivial topological structure) to 0 (trivial case in the monodomain configuration).

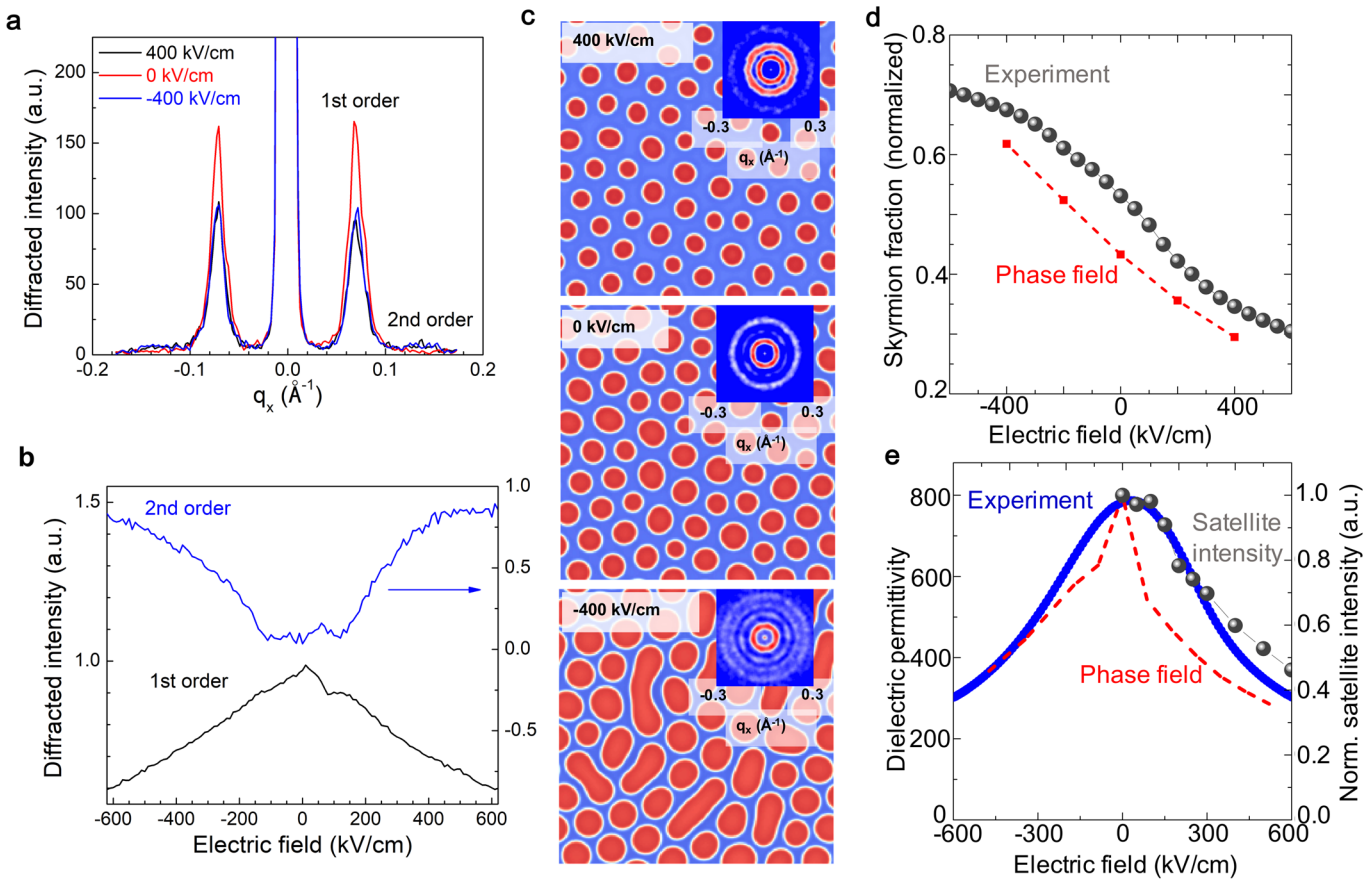

Extended Data Fig. 9 | Tunable skyrmion size under electric field as a basis for dielectric enhancement $[(SrTiO_3)_{16}/(PbTiO_3)_{16}]_8$ superlattice. **a**, Experimental line cuts through skyrmion diffuse scattering showing 1st and 2nd order satellites, including their suppression and enhancement, respectively, under external electric field. **b**, Electric field dependency of 1st and 2nd order satellites shown in **a**, determined experimentally. **c**, Phase field model of vertical polarization distribution versus electric field depicting planar cuts (80 nm × 80 nm) through the center and parallel with the $PbTiO_3$ layer. Insets show FFT averages for all $PbTiO_3$ layers of the superlattice, which indicates the emergence of 2nd order diffuse scattering skyrmion ring in addition to the dominant 1st order diffuse scattering skyrmion ring. The 2nd order ring intensity is enhanced under application of electric field relative to without field. **d**, Comparison between the experimentally estimated and phase-field calculated skyrmion areal fraction inside $PbTiO_3$ layers of the superlattice. **g**, Comparison between the experimentally measured (blue) and phase- field calculated (red) dielectric permittivity of the superlattice, which is closely mapped with electric field dependent normalized satellite intensity of skyrmion calculated from reciprocal space (dark gray, right axis).

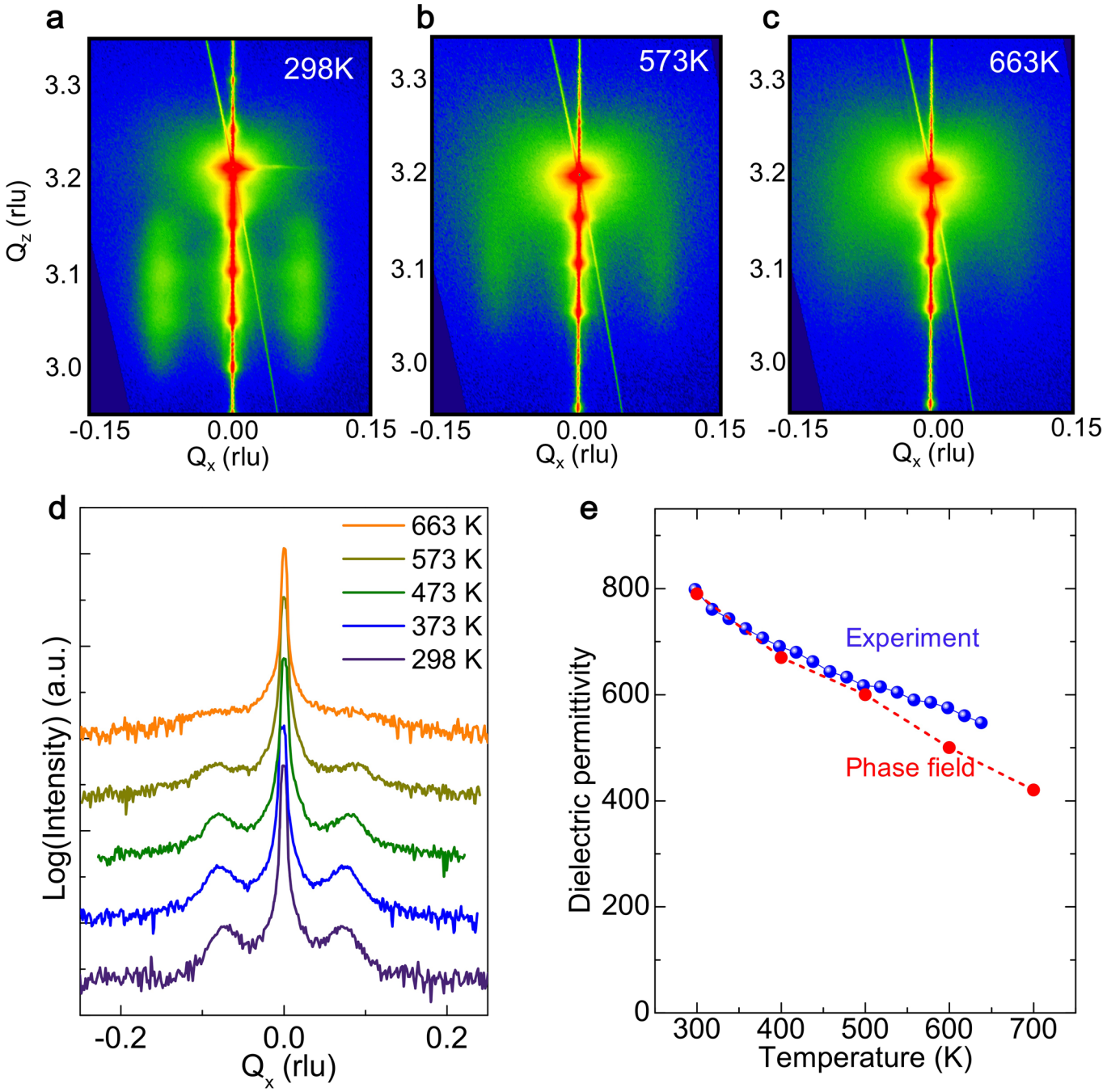

Extended Data Fig. 10 | Temperature control of skyrmion of $[(SrTiO_3)_{16}/(PbTiO_3)_{16}]_8$ superlattice. a-c, Temperature dependent three-dimensional, synchrotron-based symmetric reciprocal space mapping about the (002) diffraction condition of the $SrTiO_3$ substrate. The satellite peaks along (100) direction (side-lobes) which correspond to the skyrmions. **d**, The in-plane satellite peaks intensity (skyrmion peaks) diminishing upon heating and completely disappeared ~600K. **e**, Comparison between the temperature-dependent experimentally measured and phase- field calculated out-of-plane dielectric permittivity of the superlattice.